

Mixed Effects Deep Learning Autoencoder for interpretable analysis of single cell RNA Sequencing data

Aixa X. Andrade, Son Nguyen and Albert Montillo
Lyda Hill Department of Bioinformatics
University of Texas Southwestern Medical Center
Dallas, TX 75390, USA

Abstract

Single-cell RNA sequencing (scRNA-seq) data are often confounded due to technical or biological batch effects. Existing deep learning models aim to mitigate these effects but may inadvertently discard batch-specific information. We propose a Mixed Effects Deep Learning (MEDL) Autoencoder framework that separately models batch-invariant (fixed effects) and batch-specific (random effects) components. By decoupling fixed effects representing biological states from random effects capturing batch-specific variations, MEDL integrates both types of information into predictive models, minimizing information loss. This approach improves interpretability enabling 2D visualizations that show how the same cell would appear across different batches, facilitating exploration of batch-specific variations.

We applied MEDL to three datasets: Healthy Heart, Autism Spectrum Disorder (ASDc), and Acute Myeloid Leukemia (AML). In Healthy Heart, MEDL managed 147 batches, assessing its capacity to handle high batch numbers. In ASDc, MEDL captured donor heterogeneity between autistic and healthy individuals, while in AML, it distinguished heterogeneity in a complex setting with variable cell-type presence and malignant cells in diseased donors. These applications demonstrate MEDL's potential to capture fixed and random effects, improve visualization, and enhance predictive accuracy, offering a robust framework for cellular heterogeneity analysis across diverse datasets.

1. Introduction

Single-cell RNA sequencing provides critical insights of cellular heterogeneity by capturing gene expression variations at single-cell resolution (Hwang et al., 2018), and is widely used for analyzing biological systems. However, the non-linearity (Yousuff et al., 2024), sparsity (Bouland et al., 2023), and high dimensionality (Wu & Zhang, 2020) of scRNA-seq data pose challenges in extracting meaningful biological insights. Additionally, scRNA-seq data are often confounded by batch effects—variations introduced by different experimental conditions or biological variability (Tung et al., 2017). These batch effects can arise from biological sources, such as donor variability, or technical factors, including collection time, library preparation methods, sequencing lanes, and differences during data integration from various experiments or laboratories (Haghverdi et al., 2018; Luecken & Theis, 2019). Such batch effects hinder researchers' ability to uncover biological relationships within the data like identifying associated cell types, mapping cell trajectories, and understanding gene expression patterns.

The increasing availability of publicly accessible scRNA-seq data has intensified the demand for effective data integration across multiple batches (Hwang et al., 2024). Consequently, batch correction algorithms have gained popularity, addressing this need. Autoencoder-based deep learning methods for batch correction have become prevalent due to their ability to handle non-linearity, as well as their flexibility, and scalability. These methods offer a robust approach to transforming data into a batch-invariant space. Pioneering examples include Batch Effect ReMoval Using Deep Autoencoders (BERMUDA) (Wang et al., 2019), DESC (Li et al., 2020), variational autoencoders for single-cell gene expression data (scVAE) (Gronbech et al., 2020), and autoencoders with cell type classifiers to preserve cell type signals like AutoClass (Li et al., 2020). On the other hand, the principles of generative adversarial networks (GANs)—where a generator aims to create batch-invariant data that appears realistic, and a discriminator strives to distinguish real from fake data—have also been employed for batch correction. Moreover, GANs have been combined with autoencoders and Mutual Nearest Neighbor (MNN) pairing for enhanced batch correction. For example, iMAP integrates all cells as if they originated from an anchor batch using an adversarial paired transfer network within the GAN framework, leveraging MNN pairing to align

datasets (Wang et al., 2021). ResPAN advances this approach by introducing a residual autoencoder with skip connections and utilizing MNN pairing to guide the adversarial network across all batches without relying on an anchor (Wang et al., 2022). Building upon these adversarial frameworks, recent methods have incorporated batch classifiers and cell type classifiers to the adversarial autoencoders to further improve batch correction. scDREAMER integrates a batch classifier and offers the option of adding a cell type classifier for supervised batch correction, enhancing the preservation of biological variability while removing batch effects (Shree et al., 2023). Similarly, Integrating Multiple Single-Cell Datasets via an Adversarial Autoencoder (IMAAE) employs an anchor batch GAN-style adversarial approach combined with a cell type classifier to effectively align datasets (Wang et al., 2023). The Autoencoder-based Batch Correction (ABC) method introduces two cell type classifiers: one applied to the latent space and another to the reconstructed data. (Danino et al., 2024). Additionally, the Dynamic Batching Adversarial Autoencoder (DB-AAE) presents a novel strategy by varying the batch size during training—distinct from experimental or RNA-seq batch sizes—to enhance the model's robustness to batch effects (Ko & Sartorelli, 2024). None of these methods explicitly model the batch effects, and trying to correct the batch effects without explicitly modeling them can inadvertently discard crucial batch-specific information, especially when batches represent individual donors with biologically relevant data. This scenario is analogous to using models that include only fixed effects (Nguyen et al., 2023), which are inadequate when batch effects—akin to random effects in linear mixed-effects models—are present. Fixed-effects models concentrate solely on common signals, ignoring variability across batches or donors. We hypothesize that characterizing batch variability is important to enhance our understanding of scRNA-seq data and to make more accurate predictions of relevant biological states such as diagnoses and cell type. For example, when batch variability is experimental or technical, it can provide insights into experimental differences; when it is biological, it can reveal information about cellular heterogeneity. By precisely modeling and quantifying batch variability such methods can offer deeper biological insights and improve the interpretability.

Furthermore, Adversarial Information Factorization (AIF) addresses batch effect correction by explicitly modeling the distributions of cells conditioned on their respective batches. By learning these batch-specific distributions, AIF projects all cells onto a unified batch distribution, effectively aligning and integrating datasets across different batches (Monnier & Cournede, 2024). Furthermore, models that learn batch variability, such as AIF, *do not clearly separate batch-specific effects from dataset-invariant effects, reducing interpretability*. This lack of interpretability limits their applicability and misses opportunities in personalized medicine.

While numerous batch correction methods have been developed, most focus on removing batch effects without explicitly modeling them, *which can lead to overcorrection or loss of biologically relevant information—especially when biological signals are intertwined with batch effects* (Luecken et al., 2022). Some approaches attempt to enhance cell-type signals by incorporating cell-type labels into the integration process such as ABC or AutoClass by imposing similarity constraints (e.g., ResPAN and AIF). However, balancing effective batch correction with the retention of biological variation remains a challenge.

To address the limitations of existing methods that often discard batch-specific information, we introduce the Mixed Effects Deep Learning (MEDL) framework. Inspired by Nguyen et al. (2023), MEDL builds upon subnetworks that model both fixed effects (batch-invariant biological states) and random effects (batch or donor-specific variations) within an autoencoder tailored for scRNA-seq data. By separately capturing these complementary sources of variation, MEDL minimizes information loss and enhances interpretability.

When batch effects are purely technical, the fixed effects subnetwork preserves cell type signals. However, when batches contain biological variation—such as tissue differences or donor-specific characteristics—the fixed effects subnetwork may inadvertently remove important biological information. In these cases, the random effects subnetwork becomes crucial by capturing the discarded batch-specific variations, allowing MEDL to

recover meaningful signals that might otherwise be lost. By modeling these effects separately, MEDL provides a transparent and interpretable approach that preserves both core biological signals and batch-specific information, enhancing the accuracy of scRNA-seq analysis.

This approach not only improves classification of disease status, donor group, and cell type but also enhances interpretability by revealing the impact of batch-specific variations on cellular heterogeneity. Moreover, because our model trains the fixed and random effects subnetworks independently, it remains adaptable; existing batch correction methods that aim to generate a batch-invariant latent space such as AutoClass, ABC and scDREAMER—can be integrated into our framework as the fixed effects subnetwork, complemented by our random effects subnetwork.

We characterize our MEDL subnetworks through the following experiments: (1) We evaluate the model's ability to preserve biological signals and correct batch effects within the fixed effects latent space while modeling batch effects in the random effects latent space. By utilizing the learned batch effects, we can compare differences in a cell's scRNA dataset across batches via visual representation. (2) We demonstrate the complementary nature of the fixed and random effects subnetworks by using both latent spaces to predict targets of interest such as disease status, donor group, and cell type. (3) Inspired by models like ABC, scDREAMER, and AutoClass, we incorporate a cell-type classifier into the fixed effects subnetwork to evaluate its impact on cell-type signal preservation and batch correction, mitigating potential loss of cell type information.

2. Datasets

To create a comprehensive evaluation of our MEDL framework across diverse biological and technical contexts, we selected three datasets that span key dimensions of variability in scRNA-seq data (Table 1). These dimensions include health status (healthy individuals versus diseased patients), tissue types (heart, brain, blood cells), sources of batch effects (technical protocols, donor differences, tissue types, inclusion of cell lines), and the degree of confoundedness between cell type and batch.

The first dataset, the *Healthy Heart dataset* (Litvinukova et al., 2020; Yu et al., 2023a) consists of scRNA-seq data from heart tissues of healthy individuals. It presents multiple sources of batch variability due to the use of two different sequencing protocols (technical differences), samples from various donors, and different tissues within the heart. There is confoundedness between cell type and batch because some cell types are present only in specific tissues. This dataset allows us to assess MEDL's ability to handle a high number of batches and complex batch effects.

The second dataset, the *Autism Spectrum Disorder (ASD) and control (ASDc) dataset* (Velmeshev et al., 2019b) includes single-nuclei (sn) RNA-seq data from prefrontal cortex (PFC) and anterior cingulate cortex (ACC) brain samples. Batch effects primarily arise from donor variability between ASD and control subjects. There is indirect confoundedness between cell type and batch, as certain cell types are more affected in ASD than in controls. This dataset enables us to evaluate MEDL's capacity to capture donor heterogeneity and disease-related biological variations.

The third dataset, the *Acute Myeloid Leukemia (AML) and healthy (AMLh) dataset* (Velmeshev et al., 2019b) comprises scRNA-seq data from both healthy individuals and AML patients, as well as cell lines. Batch effects stem from donor variability, including differences between healthy and AML subjects, and cell lines. This dataset features strong confoundedness between cell type and batch: malignant cells that are only present in diseased subjects and cell lines, while healthy cells can originate from both diseased and healthy patients.

By selecting these datasets, which cover a range of health statuses (healthy, ASD, AML), tissue types (heart, brain, blood cells), and batch effect complexities, we demonstrate MEDL's versatility and robustness in handling diverse scRNA-seq data scenarios.

Data Preparation and Preprocessing

All the scRNA-seq data was preprocessed with the Scanpy library (Wolf et al., 2018) using standard preprocessing steps (Yu et al., 2023a).

The datasets were then divided into five folds for cross-validation, stratified by batch and the biological feature of interest—cell type in all three datasets. For each split, three folds were used for training, one for validation, and one for testing. The data were loaded for each subset and scaled between zero and one using min-max scaling before model fitting.

Table 1. Details of Preprocessed datasets used to evaluate MEDL models.

	<i>Healthy Heart</i> (Litvinukova et al., 2020; Yu et al., 2023b)	<i>ASD and Controls (ASDc)</i> (Velmeshev et al., 2019b)	<i>AML and healthy (AMLh)</i> (van Galen et al., 2019)
Description	Heart Cells of Different Tissues	Autism Spectrum Disorder (ASD) and Controls	Samples of Healthy and AML Subjects
Data Type	Single cell	Single nuclei	Single cell
Total Cells (Pre-Filtering)	486,134	104, 559	41,090
Total Cells (Post-Filtering)	486,134	104, 559	38,417
Total Genes	33,538	36,501	27,899
High Variable Genes	3,000	2,916	2,916
Number of Cell Types	12 + Not assigned cell type category	17	6 Malignant + 15 Healthy
Batch Effect	Batch (z =147)	Donor (z = 31)	Donor (z=19) 12 AML Donors, 5 Healthy Donors, 2 Cell Lines

Since the ASDc and AMLh datasets had previously undergone quality control, no additional cells were removed during the filtering step. For the AMLh dataset, additional quality control measures were implemented. Cells with undefined or missing cell type annotations were excluded. Furthermore, samples identified by Dai et al., (2021) as having ambiguous annotations—specifically AML314, AML371, AML722B, and AML997 (Dai et al., 2021)—were removed from the original 16 AML donors to ensure the dataset's integrity, resulting in 12 AML donors available for analysis. The ASDc dataset had previously undergone a log2 transformation as part of the original preprocessing by van Galen et al. (2019). To maintain consistency across all datasets, this transformation was reversed by applying an exponential function (base 2) to the data after adding 1 to each value, thereby returning the data to its original scale. Following this reversal, the standard preprocessing pipeline was applied.

3. Methods

3.1. MEDL Framework for scRNA-seq data

When data is confounded by batch effects, as commonly observed in single-cell RNA sequencing (scRNA-seq) data, it is essential to employ methods that account for these confounders. The Mixed Effects Deep Learning (MEDL) framework addresses this need by extending linear mixed-effects models (Vestal et al., 2022) into a nonlinear context. A linear mixed-effects model is defined as:

$$y_i = x_i^T \beta_i + x_i^T u_j + \epsilon_i$$

In this equation, y_i represents the target variable, x_i^T is the gene expression vector of the i^{th} cell, β_i denotes the fixed effects intercepts and weights capturing batch invariant trends across all samples, u_j signifies the random effects intercepts and weights accounting for variability of the batches j (assumed to follow a normal distribution $N(0, \sigma_j)$), and ϵ_i is the residual error term. Building upon this foundation, the MEDL framework extends the model into a nonlinear context, effectively addressing the inherent non-linearity from confounded scRNA-seq data.

MEDL Model Architecture

Our Mixed Effects Deep Learning Autoencoder (MEDL-AE) framework for single-cell RNA sequencing (scRNA-seq) data captures both fixed and random effects within gene expression vectors of individual cells. Fixed effects represent batch invariant features, while random effects account for batch or donor-specific variations. The model processes a gene expression count matrix $X \in \mathbb{R}^{n \times m}$, where n is the number of cells and m is the number of genes, the model outputs a gene expression matrix \hat{X} and latent space representations derived from the encoder.

The model architecture of our framework comprises two parallel subnetworks: one which captures the fixed effects and another for the random effects (Fig. 1). The fixed effects subnetwork (MEDL-AE-FE) is designed to suppress batch effects. It consists of an autoencoder (AE) with weight tying between encoder and decoder, two dense hidden layers, and an adversarial classifier that learns to predict the batch labels z .

The fixed effects loss function L_{FE} is given by:

$$L_{FE}(X, \hat{X}, z, \hat{z}): \lambda_{MSE} L_{MSE}(X, \hat{X}) - \lambda_A L_{CCE}(z, \hat{z})$$

Here, λ_{MSE} and λ_A balance the reconstruction and adversarial losses, respectively. The mean squared error (MSE) measures the reconstruction error:

$$L_{MSE}(X, \hat{X}) = \frac{1}{n} \sum_{i=1}^n \|X_i - \hat{X}_i\|^2$$

where X_i and \hat{X}_i are the original and reconstructed gene expression vectors of cell i . The categorical cross-entropy (CCE) quantifies the adversarial classifier's performance:

$$L_{CCE}(z, \hat{z}) = -\frac{1}{n} \sum_{i=1}^n \sum_{k=1}^K z_{i,k} \log \hat{z}_{i,k}$$

where $z_{i,k}$ is the true label (one-hot encoded) and $\hat{z}_{i,k}$ is the predicted probability for class k for cell i . Optimizing L_{FE} enables the model to effectively capture fixed effects while mitigating batch-specific variations.

The random effects subnetwork models the distribution of batch-specific variations using variational inference (Blei et al., 2017). The true batch distributions $p(U|X)$ with $U = \{u_j\}$ are approximated by an optimized surrogate posterior $q(U)$. Each batch prior $p(U)$ is represented as a normal distribution centered at zero.

The objective function involves maximizing the Evidence Lower Bound (ELBO), which can be expressed as:

$$ELBO = E_{q(U)}[\log p(X|U)] - D_{KL}(q(U) \parallel p(U))$$

Maximizing the ELBO is equivalent to minimizing the Kullback–Leibler (KL) divergence D_{KL} between the surrogate posterior $q(U)$ and the true posterior $p(U|X)$, up to an additive constant $p(X)$:

$$D_{KL}(q(U) \parallel p(U|X)) = \log p(X) - ELBO$$

The expected log-likelihood $E_{q(U)}[\log p(X|U)]$ represents the model's fit to the data and is implemented using suitable loss functions. In this work, a combination of MSE for data reconstruction and CCE for batch classification is used:

$$-E_{q(U)}[\log p(X|U)] \approx \lambda_{RE_1} L_{MSE}(X, \hat{X}') + \lambda_{RE_2} L_{CCE}(z, \hat{z}')$$

Here, \hat{X} and \hat{z}' are the reconstructed gene expression matrix and predicted batch labels from the random effects subnetwork. The term $\log p(X)$ is constant with respect to U and can therefore be ignored during optimization.

The total loss function for the random effects subnetwork L_{RE} is:

$$L_{RE}(X, \hat{X}', z, \hat{z}',) : \lambda_{MSE} L_{MSE}(X, \hat{X}') + \lambda_{CCE_z} L_{CCE}(z, \hat{z}') + \lambda_{KL} D_{KL}(q(U) \parallel p(U))$$

where λ_{MSE} , λ_{CCE_z} and λ_{KL} are the weights of the L_{MSE} , L_{CCE} and D_{KL} loss terms, respectively. The first term ensures the latent representation facilitates accurate reconstruction, the second term enforces the latent space to encode batch-specific information, and the third term regularizes the model to prevent overfitting by constraining the learned distribution to align with the prior.

The Kullback–Leibler (KL) divergence between two univariate Gaussian distributions $q(u_j) = N(\mu_q, \sigma_q^2)$ and $p(u_j) = N(\mu_0, \sigma_0^2)$ is given by:

$$D_{KL}(q(u_j) \parallel p(u_j)) = \int_{-\infty}^{\infty} q(u) \log \frac{q(u_j)}{p(u_j)} du$$

In a more explicit form, the KL divergence over all batches j can be written as:

$$D_{KL}(q(U) \parallel p(U)) = \frac{1}{2} \sum_j \left[\log \left(\frac{\sigma_j^2}{\sigma_0^2} \right) - 1 + \frac{\sigma_0^2 + (\mu_j - \mu_0)^2}{\sigma_j^2} \right]$$

where μ_j and σ_j^2 are the mean and variance of $q(u_j)$, and $\mu_0 = 0$ and σ_0^2 are those of the prior $p(u_j)$.

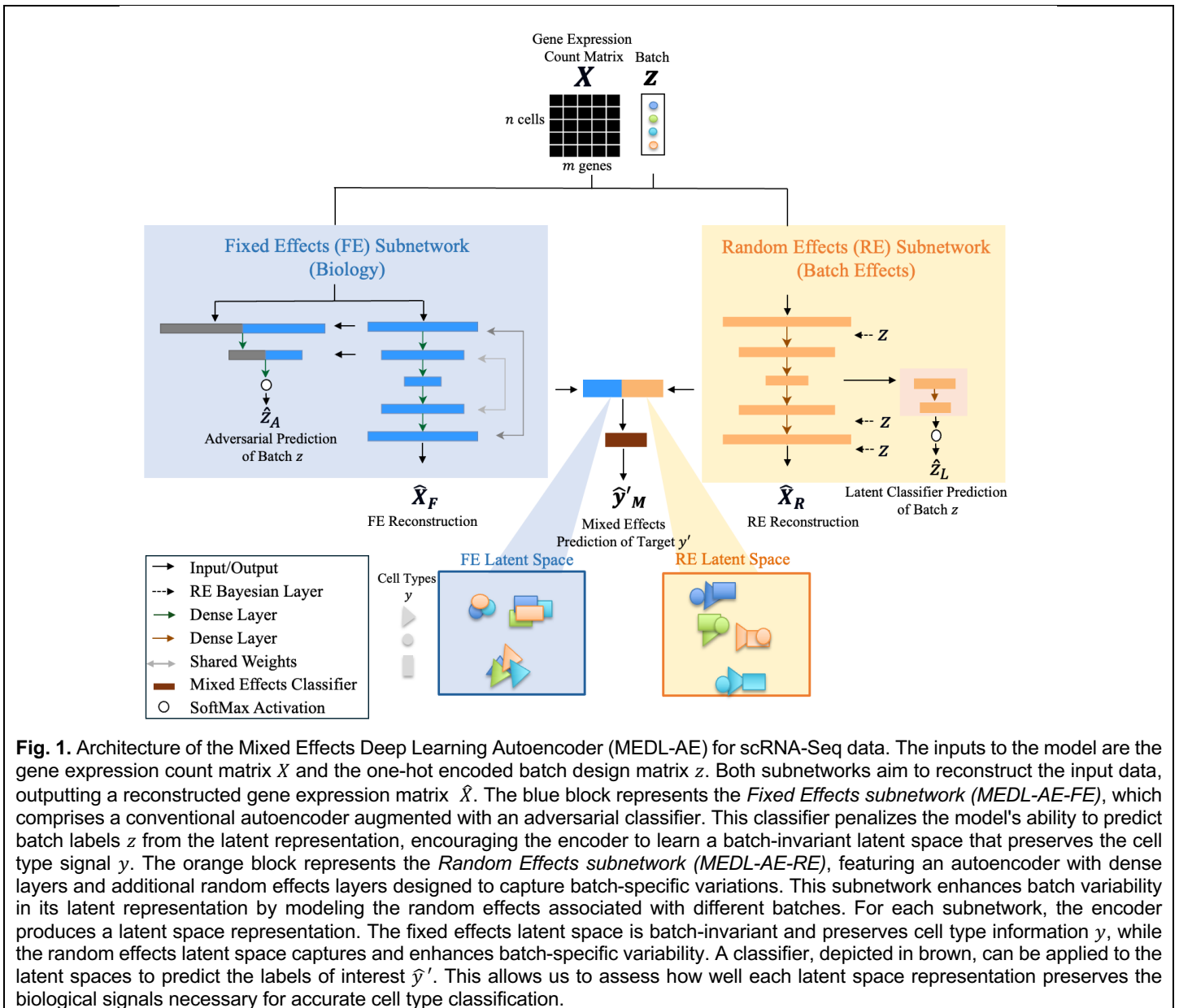


Fig. 1. Architecture of the Mixed Effects Deep Learning Autoencoder (MEDL-AE) for scRNA-Seq data. The inputs to the model are the gene expression count matrix X and the one-hot encoded batch design matrix z . Both subnetworks aim to reconstruct the input data, outputting a reconstructed gene expression matrix \hat{X} . The blue block represents the *Fixed Effects subnetwork (MEDL-AE-FE)*, which comprises a conventional autoencoder augmented with an adversarial classifier. This classifier penalizes the model's ability to predict batch labels z from the latent representation, encouraging the encoder to learn a batch-invariant latent space that preserves the cell type signal y . The orange block represents the *Random Effects subnetwork (MEDL-AE-RE)*, featuring an autoencoder with dense layers and additional random effects layers designed to capture batch-specific variations. This subnetwork enhances batch variability in its latent representation by modeling the random effects associated with different batches. For each subnetwork, the encoder produces a latent space representation. The fixed effects latent space is batch-invariant and preserves cell type information y , while the random effects latent space captures and enhances batch-specific variability. A classifier, depicted in brown, can be applied to the latent spaces to predict the labels of interest \hat{y}' . This allows us to assess how well each latent space representation preserves the biological signals necessary for accurate cell type classification.

The MEDL hyperparameters are described in Tables S1–S3. In the fixed effects subnetwork, we employed two Adam optimizers: one dedicated to training the adversarial classifier alone, and the other optimizing the total loss of the subnetwork. In contrast, the random effects subnetwork was trained using a single Adam optimizer. Early stopping based on validation loss was utilized throughout as a regularization strategy to prevent overfitting.

Comparable, Complementary and Auxiliary Models

To rigorously evaluate the performance of the MEDL models, we incorporated comparable models that are widely used in scRNA-seq analysis, as well as auxiliary models to further validate our approach. Principal Component Analysis (PCA), a standard method for dimensionality reduction in scRNA-seq, was implemented using scikit-learn (Pedregosa et al., 2015) and served as a baseline for comparison. While PCA provides linear dimensionality reduction, it does not explicitly address batch effect correction, making it a useful reference point. To overcome PCA's linearity limitation, we included a standard Autoencoder (AE) as a nonlinear alternative. This model served as both an ablation test for the MEDL-AE-FE model and as a complementary nonlinear dimensionality reduction method to PCA.

To evaluate the complementary nature of the two subnetworks (fixed and random effects), we employed a Random Forest classifier (Breiman, 2001) from scikit-learn with default hyperparameters (Pedregosa et al., 2015) to classify the target labels based on the latent representations from the fixed effects subnetwork (MEDL-AE-FE) and the combined latent spaces from the full MEDL-AE model. The Random Forest model was chosen because it is interpretable, effectively handles both linear and nonlinear relationships and it is not prone to overfitting. We used the same 5-fold cross-validation partitioning scheme described for preprocessing the data input for the MEDL subnetworks. The PCA latent space was also utilized as a comparative baseline. This approach enabled us to assess how the integration of both fixed and random effects enhances classification performance compared to using fixed effects alone.

Furthermore, when cell-type labels are available or can be estimated for certain datasets, an approach to leveraging this information is to use an Autoencoder Classifier (AEC). To ensure a comprehensive evaluation, we included this model in our comparisons.

The MEDL Autoencoder (AE) model can be complemented with a latent classifier to enhance the cell-type signal, thereby forming the fixed effects classifier subnetwork (MEDL-AEC-FE). This subnetwork predicts the one-hot encoded labels y by incorporating a categorical cross-entropy term $L_{CCE}(y, \hat{y})$ into the fixed Effects loss, weighted by λ_{CCE_y} . The updated fixed effects loss function L_{FE} becomes:

$$L_{FE}(X, \hat{X}, z, \hat{z}, y, \hat{y}) = \lambda_{MSE} L_{MSE}(X, \hat{X}) - \lambda_A L_{CCE}(z, \hat{z}) + \lambda_{CCE_y} L_{CCE}(y, \hat{y})$$

Additionally, an Autoencoder Classifier (AEC) with an architecture similar to AutoClass (Li et al., 2022) was included as an ablation test for the MEDL-AEC-FE model. This facilitated the evaluation of the specific contribution of the classifier to cell type signal preservation and batch correction.

3.2. Performance Metrics

The core metric used to guide our MEDL training was the validation total loss for each of the subnetworks which is described in equations 1 and 2. Additionally, clustering metrics were used to evaluate the biological separability, batch correction, and batch modeling.

Metrics to characterize cell type separability, batch correction, and batch modeling

To assess the effects of the MEDL subnetworks on cell type separability, batch correction, and batch modeling, we utilized three internal clustering metrics: Average Silhouette Width (ASW) (Rousseeuw, 1987), Calinski-Harabasz (CH) index (Calinski & Harabasz, 1974), and Davies-Bouldin (DB) index (Davies & Bouldin, 1979), to assess the effects of the MEDL subnetworks on cell type separability, batch correction, and batch modeling. These metrics have been widely used in scRNA-seq data analysis (Li et al., 2021; Ning et al., 2023; Wang et al., 2024), with ASW being the most popular among them (Hu et al., 2024; Luecken et al., 2022; Shree et al., 2023; Yu et al., 2022; Yu et al., 2023a).

We selected ASW as our primary metric due to its popularity, robustness to clusters of arbitrary shapes (Vendramin et al., 2010) and because its values range from -1 to 1, facilitating comparisons across methods and datasets. Unlike the CH and DB indices, which assume convex or spherical clusters and focus on variance structure and cluster overlap, respectively, ASW does not rely on such assumptions. It provides a balanced assessment of cohesion and separation without sensitivity to cluster shape or size, making it well-suited for the

complex structures often observed in scRNA-seq data. By including CH and DB indices, we ensured a comprehensive evaluation from different perspectives: CH captures variance structure and compactness, while DB highlights the degree of overlap between clusters.

We computed these scores using both cell type and batch labels for cell samples, capped at 10,000 per fold (training, validation, or test). Biological separability was measured using cell type labels from the original publications: ASDc dataset (Velmeshev et al., 2019b), Healthy Heart dataset (Yu et al., 2023b), and AMLh dataset (van Galen et al., 2019).

To align the interpretation of the DB index with the CH index and ASW, we used its reciprocal ($1/DB$), ensuring that higher scores consistently indicate better clustering quality. For cell types, higher scores signify improved separability in the latent space, enhancing the cell type signal—the primary objective of batch correction. Conversely, lower scores for batches indicate more effective batch correction, as batches become less distinguishable, reflecting improved batch mixing. Additionally, higher batch scores in the random effects subnetwork suggest effective capture of between-batch variance in gene expression data.

Classification Performance Metrics

To evaluate the classification performance of predicting labels from the MEDL latent spaces, we calculated accuracy, balanced accuracy, and chance accuracy. For chance accuracy, we employed scikit-learn’s Dummy Classifier with the stratified strategy, which generates random predictions while maintaining the original class distribution in the dataset (Pedregosa et al., 2015). This provides a more realistic baseline for comparison, as it accounts for the imbalanced nature of the classes rather than assuming uniform distribution, thus offering a more appropriate measure of chance-level performance. These metrics range between 0 and 100%. Balanced accuracy accounts for class imbalance, which is crucial in our datasets due to multiple cell type classes with varying abundances.

In the results section, we report test results for ASW, classification accuracy, balanced accuracy and chance accuracy.

3.3. Hyperparameter Optimization

The MEDL model comprises two subnetworks—the fixed effects subnetwork and the random effects subnetwork—each with multiple hyperparameters detailed in Tables S1–S3. All hyperparameters, except for the weights assigned to individual loss terms, were kept constant across all base models and ablation tests. The total loss function is constructed as a sum (or difference) of individual loss terms, each multiplied by its specific weight hyperparameter, thereby controlling the contribution of each loss term to the overall loss function.

To select the weights of the individual loss terms, we employed a manual, case-by-case strategy using training and validation folds from the 5-fold cross-validation detailed in the preprocessing section. Our primary objective was to ensure proper optimization and prevent any single component—such as the adversarial loss—from dominating the training process. Specifically, we ensured that the reconstruction loss remained of the same order of magnitude, or greater, than the other loss terms. This involved running the model for several epochs and monitoring the contribution of each loss term to the total loss function. Adjustments were made to the weights so that none of the adversarial, cell type classifier, batch classifier, or KLD losses exceeded the reconstruction loss during the initial epochs of training. By maintaining this balance, we facilitated proper optimization across all components.

Due to the variation in the number of batches across datasets, the loss weights for the adversarial and reconstruction components were adjusted accordingly, as illustrated by the training curves (Fig. S5–S10). For the ASDc and AMLh fixed effects subnetworks, we performed additional hyperparameter optimization to maximize cell type separability in the latent spaces using the ASW for cell type. Using our manual, case-by-case approach, we increased the reconstruction loss weight relative to the adversarial loss whenever the cell type signal diminished.

Early stopping based on validation loss was utilized throughout as a regularization strategy to prevent overfitting. In summary, our hyperparameter selection involved carefully balancing the weights of the loss terms, using training and validation folds from the 5-fold cross-validation strategy, and applying early stopping to ensure robust and generalizable models.

For evaluation and visualization purposes, the latent space of all models was encoded into a two-dimensional vector for each data cell, resulting in an $(n, 2)$ matrix where n is the number of cells. This two-dimensional latent representation allows us to effectively visualize and evaluate the model's performance.

3.4. Visualization Methods

We used Uniform Manifold Approximation and Projection (UMAP) (McInnes et al., 2018) visualizations of the models latent spaces to provide a more comprehensive evaluation of the model's performance. This combined approach allows us to better assess both cell-type signal enhancement and batch mixing. We generated UMAP visualizations using Scanpy UMAP tools (Wolf et al., 2018).

Genomaps for 2D visualization of individual cells

Genomaps (Islam & Xing, 2023) provide a 2D representation of gene expression profiles for each cell by arranging genes on a 2D grid according to their gene-to-gene interactions. In this layout, genes positioned at the same distance r from the center exhibit equivalent levels of gene-to-gene interaction. Importantly, this method preserves the original gene expression values while organizing the genes spatially, allowing for a clear visualization of the relationships between genes and providing insights into batch effects. Islam and Xing et al. (2023) demonstrated that Genomaps can create gene expression patterns specific to cell types. We visualized batch variability as Genomaps specific patterns.

3.5. Experiments

3.5.1. Experiment 1: Characterization of the fixed and random effect latent spaces and visualizing learned batches

We conducted two analyses to understand the performance and interpretability of the proposed MEDL approach. First, we assessed the latent spaces of the two MEDL subnetworks quantitatively and qualitatively by: (a) evaluating cell type separability, batch correction, and batch modeling, and (b) assessing the interpretability of the FE and RE subnetworks by visualizing gene expression reconstructions in 2D genomaps (Islam & Xing, 2023), representing individual cells.

a) Evaluation of cell type separability, batch correction and batch modeling

To demonstrate that the fixed effects subnetwork (MEDL-AE-FE) and the random effects subnetwork (MEDL-AE-RE) learn complementary information, we assessed their ability to transform input data into batch-invariant and batch-specific latent spaces, respectively. The fixed effects subnetwork is designed to map the input to a

batch-invariant space, enhancing cell type separability. We evaluated this by calculating the Adjusted Silhouette Width (ASW) for cell type in the latent space derived from its encoder; a higher ASW indicates better separability.

We also measured the degree of batch correction in the fixed effects subnetwork using the ASW for batch, where a lower ASW signifies effective removal of batch effects. Conversely, in the random effects subnetwork, an increase in the ASW for batch suggests successful modeling of batch-specific distributions. Latent spaces were obtained from the encoder outputs of each subnetwork.

To ensure robust estimates, we employed 5-fold cross-validation to calculate the mean ASW and 95% confidence intervals across folds. Given the computational complexity of ASW calculations, we used a random sample of 10,000 cells when datasets exceeded this size in training, validation, or testing subsets. For baseline comparisons, we also computed latent spaces using Principal Component Analysis (PCA) and a standard Autoencoder (AE).

b) Assessment of the FE and RE subnetworks interpretability

To demonstrate the unique capabilities of our Mixed Effects Deep Learning Autoencoder (MEDL-AE) in addressing critical biological and clinical "what if" questions—an advantage not offered by traditional methods—we utilized both the Fixed Effects (FE) and Random Effects (RE) subnetworks to visualize gene expression patterns under different conditions. Specifically, we reconstructed gene expression count matrices using both subnetworks. The FE subnetwork transforms input data into a batch-invariant space, revealing gene expression patterns common across all batches. In contrast, the RE subnetwork captures batch-specific variations, allowing us to simulate how gene expression profiles would appear if cells originated from a different batch or donor.

By modifying the one-hot encoded batch vectors in the RE subnetwork, we projected cells into different batches or conditions. This projection capability enabled us to explore variability between different donors or experimental conditions, effectively answering pertinent biological questions such as how gene expression changes when a cell is subjected to different batch effects or disease states.

To facilitate this exploration, we selected cells from specific batches and cell types of interest, ensuring that each batch of interest was represented by at least one cell. The remaining cells were randomly chosen from the relevant cell types, resulting in a total of 300 cells per reconstructed count matrix. We combined the reconstructed gene expression data from the Autoencoder (AE), MEDL-AE-FE, MEDL-AE-RE, and the counterfactual reconstructions from MEDL-AE-RE—where cells are projected into different batches—to form a synthetic count matrix. After standard scaling this matrix, we computed the Genomap visualization using the Genomap software. This process enabled a detailed visualization of gene expression patterns, highlighting both the effects of batch correction and the underlying biological signals. It allowed us to understand batch-specific effects and assess the consistency of cell type characteristics across different experimental conditions.

By leveraging this projection capability, our method allows researchers to simulate and visualize how gene expression profiles change under different conditions, providing valuable insights into biological variability and disease mechanisms. This demonstrates the unique advantage of our approach in answering complex biological and clinical questions that are not accessible through conventional techniques.

For instance, in the Healthy Heart dataset, we focused on four cell types of interest—Pericytes, Endothelial Cells, Fibroblasts, and Ventricular Cardiomyocytes—across four different batches. By projecting cells into different batches using the RE subnetwork, we examined how gene expression profiles vary between batches and cell types.

In the ASDc dataset, we investigated differences between autistic and healthy individuals by visualizing L2/3 excitatory neurons from three control donors and three autistic donors. We selected L2/3 excitatory neurons because they exhibit the highest number of differentially expressed genes between autistic and control subjects (Velmeshev et al., 2019b). By projecting cells from healthy donors onto the autistic condition—and vice versa—we explored potential alterations in gene expression associated with autism. This not only provided insights into disease-specific gene expression patterns but also demonstrated the model's ability to simulate clinical scenarios.

Similarly, in the AMLh dataset, we visualized healthy and malignant Monocytes from healthy donors, diseased donors, and cell lines. Utilizing the RE subnetwork to project cells across different conditions, we demonstrated that our MEDL-AE-RE model effectively captures variations associated with disease states. This capability is crucial for understanding the gene expression changes underlying malignancy and could potentially aid in identifying therapeutic targets.

3.5.2. Experiment 2: Evaluate the complementary nature of the FE and RE latent representations for enhancing prediction performance

The aim of this experiment is to leverage the complementary nature of the Fixed Effects (Islam & Xing, 2023) (FE) and Random Effects (RE) latent representations to enhance label prediction. The FE subnetwork (MEDL-AE-FE) corrects batch effects by transforming gene expression data into a batch-invariant space, while the RE subnetwork (MEDL-AE-RE) captures the variability between batches. Our goal is to demonstrate that quantitatively modeling batch effects, rather than discarding them—as other batch correction methods do—adds value to the prediction process.

To assess the complementary nature of the fixed and random effects latent spaces, we utilized the latent representations from MEDL-AE-FE and MEDL-AE-RE obtained in Experiment 1. We trained a Random Forest classifier using three different input sets: (1) the latent space from MEDL-AE-FE alone, (2) the principal component analysis (PCA) components as a baseline, and (3) the concatenated latent spaces of MEDL-AE-FE and MEDL-AE-RE, thereby combining both fixed and random effects representations. Prior to training, all latent spaces were standardized, adjusting each to have a mean of 0 and a standard deviation of 1, to ensure comparability across input sets.

Since all three datasets included cell type labels (van Galen et al., 2019; Velmeshev et al., 2019b; Yu et al., 2023b), we used cell type as the primary target for classification. In the AMLh dataset, malignant and healthy cells from the same cell type were treated as two distinct cell type labels. Additionally, we conducted experiments using alternative target variables. On the AMLh dataset we used Patient Group—which includes diseased (AML patients), healthy donors, and cell line classes—as the target variable to assess the model's capability to differentiate among these groups. On the ASDc dataset we used disease status (autism spectrum disorder or control) as the target variable to evaluate the model's ability to distinguish between diseased and healthy individuals.

To ensure consistency in our evaluation, we employed the same 5-fold cross-validation splits as in Experiment 1 for all classification tasks.

3.5.3. Experiment 3: Quantification of the impact of a cell type classifier on batch and cell type separability

When cell type labels are available, this information can be leveraged by an autoencoder classifier to further ensure preservation of the cell type information in the latent representation. The autoencoder classifier aims to construct a latent representation that simultaneously has low reconstruction error and high cell classification performance. See Comparable, Complementary and Auxiliary Models section from Methods. To investigate how an autoencoder cell type classifier impacts the trade-off between batch correction and cell type preservation, we constructed a MEDL-AEC. In this case our FE model became a MEDL-AEC-FE model while our RE model did not need to change, since its goal was to construct a latent space predictive of batch. Then we evaluated the impact of the latent space classifier on cell type and batch separability, and whether these effects were driven by the classifier itself or by the adversarial component. Therefore, we compared the performance of MEDL-AEC-FE against the baseline AEC model. We used the same data partitioning splits of Experiment 1a which uses 5-fold cross-validation, and we computed the mean ASW for batch and cell type, along with 95% confidence intervals, across the five folds.

3.6. Implementation

All deep learning models were developed using TensorFlow 2.3 (Martín Abadi et al., 2015) and trained on Nvidia Tesla V100 GPUs with 32 GB of memory and Tesla P4 GPUs with 8 GB of memory. However, the fixed effects subnetworks and autoencoder models were less computationally intensive and could be trained on simpler hardware, such as the Tesla P4 GPU with 8 GB of memory. We calculated the ASW, DB, CH, accuracy, balanced accuracy, and chance accuracy using the Scikit-learn package (Pedregosa et al., 2015). ScRNA-seq preprocessing and UMAP computations (McInnes et al., 2018) were performed using the Scanpy library (Wolf et al., 2018).

4. Results

The following sections present the results of the three experiments. For each experiment the results are presented for the Health Heart, ASDc, and AMLh datasets.

Experiment 1: Characterization of the fixed and random effect latent spaces and visualizing learned batches

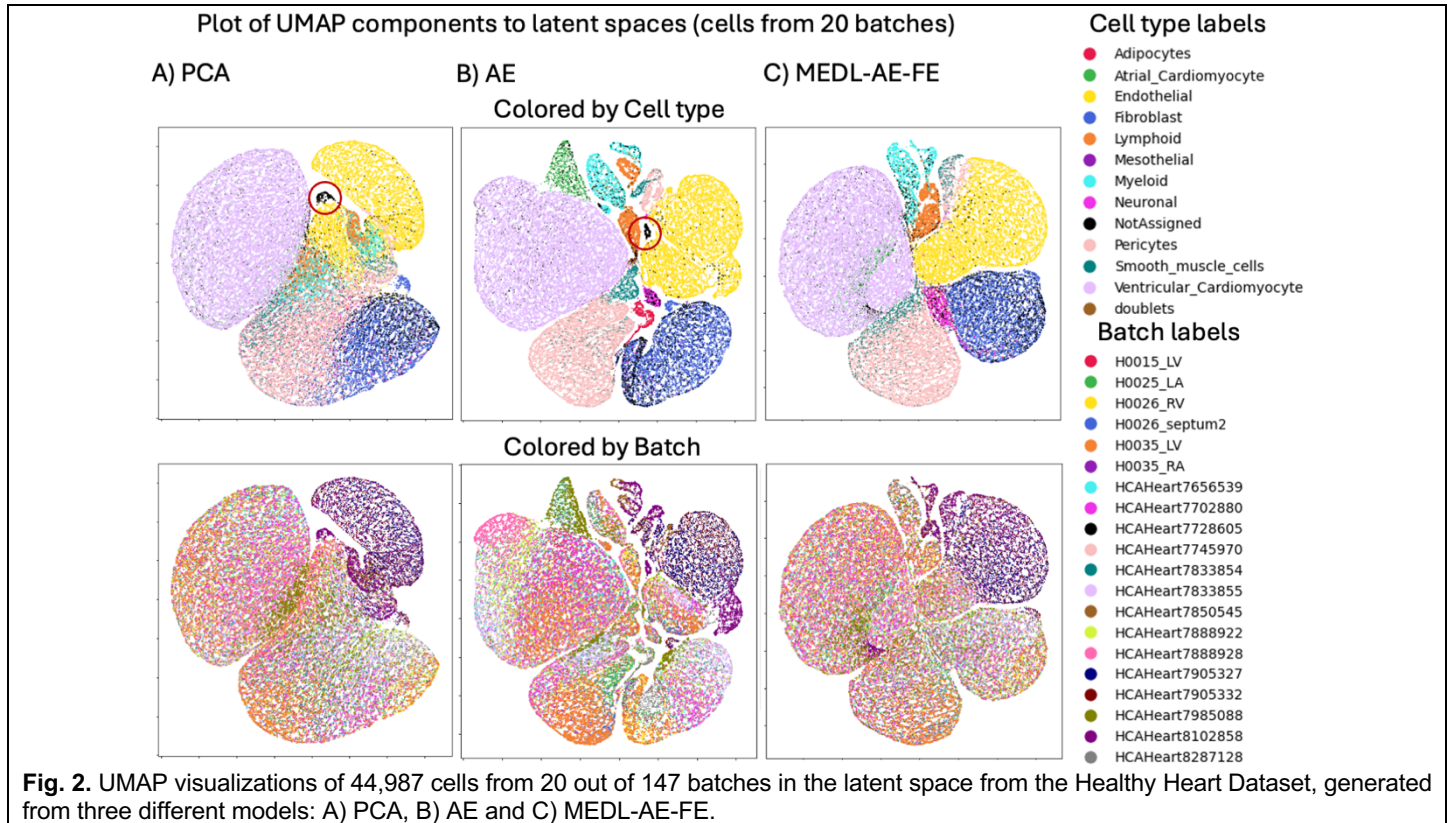
a) Evaluation of cell type separability, batch correction and batch modeling

Healthy Heart dataset

Table 2 presented the mean Average Silhouette Width (ASW) scores for batch and cell type separability across five folds of the Healthy Heart dataset, comparing latent spaces generated by the PCA, AE, MEDL-AE-FE, and MEDL-AE-RE models. PCA was the baseline model, as it was often used in scRNA-seq analysis to reduce dimensionality. Similarly, the AE was included as it was also a commonly used method for dimensionality reduction. PCA provided a baseline ASW of -0.48, and it was observed that the proposed method both suppressed batch separability, with the MEDL-AE-FE attaining -0.50 (more negative

	ASW (batch)			ASW (cell type)		
	mean	95% CI		mean	95% CI	
PCA (Baseline)	-0.48	-0.51	-0.46	-0.05	-0.06	-0.05
AE	-0.45	-0.48	-0.43	0.19	0.15	0.23
MEDL-AE-FE	-0.50	-0.52	-0.48	0.16	0.09	0.23
MEDL-AE-RE	0.37	0.16	0.58	-0.28	-0.45	-0.11

is less separable), and learned the batch effect, with the MEDL-AE-RE attaining an ASW of 0.37 (Table 2) and forming clusters separable by batch (Fig. S2, Table S7). This demonstrated the power of the proposed approach to reduce dimensionality while both suppressing and modeling the batch effect, whereas other approaches, such as the AE, merely had one effect (dimensionality reduction). The MEDL-AE-FE (-0.50) also suppressed batch effect better than the AE (-0.45). Regarding cell type separability, the PCA approach gave a baseline of -0.05. It was seen that both the AE and MEDL-AE-FE substantially improved cell type separability compared to the PCA (Table 2 and S7).



These trends were also evident in the latent space visualizations of these models (Fig. 2). In particular, we applied UMAP (McInnes et al., 2018) to 44,987 cells from 20 batches selected randomly out of 147 batches. In the first row, which depicted the batch separability of the methods, we observed that the MEDL-AE-FE model had the most uniform distribution of batches (colors), while the AE had many discernable batches (colored regions), in agreement with Table 2. In the second row, which contrasted cell-type separability, the AE and MEDL-AE-FE both showed many discernable cell types, much more so than PCA.

Cells labeled as "Not Assigned" by Yu et al., 2023 (Yu et al., 2023b) meaning they could not be assigned to any known cell type—were dispersed in the MEDL-AE-FE latent representation (Fig. 3C), reflecting their heterogeneity. In contrast, these unassigned cells formed a small cluster (circled) in the AE and PCA representations (Fig. 2A and B), which was likely a false positive since they were not expected to cluster together. This observation indicated that while AE and PCA could amplify signal, they might also amplify noise. Additionally, when using the MEDL-AE-FE model, atrial cardiomyocytes were dispersed alongside ventricular cardiomyocytes. We attributed this to the removal of batch effects—a combination of variations due to tissue type, donor, and protocol. By eliminating some of the tissue variability information, both types of cardiomyocytes appeared to merge. By comparing the AE representation to the MEDL-AE-FE representation, we identified which cell types were batch-invariant, thereby enhancing the explainability of our model.

In the ASDc dataset, the MEDL-AE-FE latent space improved the cell type signal compared to PCA, as evidenced by more defined boundaries for Myeloid, Lymphoid, Pericytes, and Smooth Muscle cells (Fig. 3). Although the ASW batch scores of MEDL-AE-FE were not higher than those of PCA, Fig. 3 demonstrated an equivalent degree of batch mixing between the two methods.

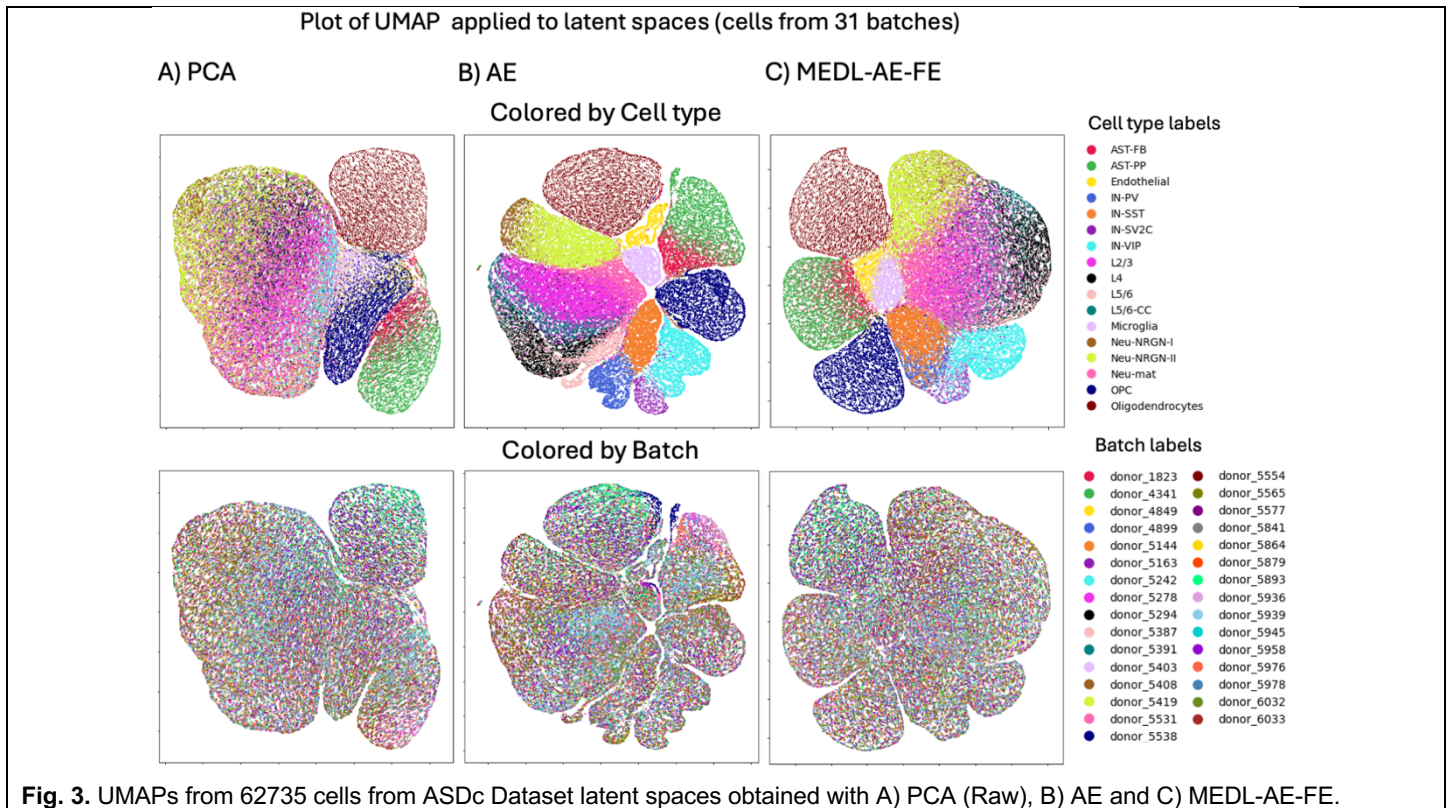
Table 3. Average Silhouette Width (ASW) scores (Mean and 95% CI across 5 folds) for batch and cell type separability in the latent spaces of the ASDc Dataset, using PCA, AE, MEDL-AE-FE, and MEDL-AE-RE models.

The nonlinear properties of the AE component in MEDL-AE-FE best preserved the cell type signal (Table S5). The total loss was calculated as the reconstruction loss minus the adversarial loss. Therefore, increasing the weight of the reconstruction loss reduced the adversarial contribution to the total loss, which lowered batch correction but enhanced the cell type signal. We selected the MEDL-AE-FE model with a higher reconstruction loss weight because it exhibited the strongest cell type signal while effectively mitigating some batch effects (Table 3 and Fig. 3).

	ASW (batch)			ASW (cell type)		
	mean	95% CI		mean	95% CI	
PCA (Baseline)	-0.31	-0.33	-0.30	0.07	0.06	0.08
AE	-0.22	-0.23	-0.20	0.33	0.31	0.36
MEDL-AE-FE	-0.23	-0.26	-0.21	0.20	0.16	0.23
MEDL-AE-RE	-0.11	-0.49	0.27	-0.19	-0.28	-0.10

By comparing the latent spaces of the AE and the MEDL-AE-FE models on the ASDc dataset (Fig. 3B and C), we identified neuron types that exhibited donor heterogeneity. For instance, Parvalbumin interneurons—which Velmeshev et al., 2019 reported to be dysregulated in patients with epilepsy and ASD—formed a distinct cluster in the AE latent space but became dispersed in the MEDL-AE-FE representation (Velmeshev et al., 2019a). This dispersion suggested that the MEDL-AE-FE model effectively removed donor-specific effects. Similarly, certain excitatory neurons, such as layer 2/3 (L2/3) and layer 5/6 corticocortical (L5/6CC) neurons—which were dysregulated in ASD compared to controls—also became dispersed among other layer neurons in the MEDL-AE-FE latent space. In contrast, oligodendrocytes and oligodendrocyte precursor cells (OPCs) exhibited minimal donor heterogeneity, indicating that their latent representations were largely unaffected by donor-specific variability. This distinction highlighted the model's ability to learn a donor-invariant latent space, thereby enhancing the interpretability of our findings.

The MEDL-AE-RE showed an increase in the ASW, 1/DB, and CH batch scores compared to other models (Table 3, Table S8), indicating its ability to capture batch effects (Fig. S3).



AMLh dataset

The AMLh dataset exhibited substantial variation in cell type representation across donors, introducing a cell type–donor confounding factor (Fig. S1). Additionally, malignant cell types were exclusively present in donors with the disease and in cell lines. Consequently, even though the MEDL-AE-FE model was more effective at recovering cell type signals compared to PCA, it showed a reduction in cell type signal relative to the AE (Table 4 and Fig. 4).

Table 4. Average Silhouette Width (ASW) scores (Mean and 95% CI across 5 folds) for batch and cell type separability in the latent spaces of the AMLh dataset, using PCA, AE, MEDL-AE-FE, and MEDL-AE-RE models.

	ASW (batch)			ASW (cell type)		
	mean	95% CI		mean	95% CI	
PCA (Baseline)	-0.28	-0.29	-0.28	-0.09	-0.09	-0.08
AE	-0.19	-0.21	-0.17	0.03	0.02	0.05
MEDL-AE-FE	-0.30	-0.31	-0.28	-0.05	-0.07	-0.04
MEDL-AE-RE	0.32	0.23	0.42	-0.36	-0.45	-0.28

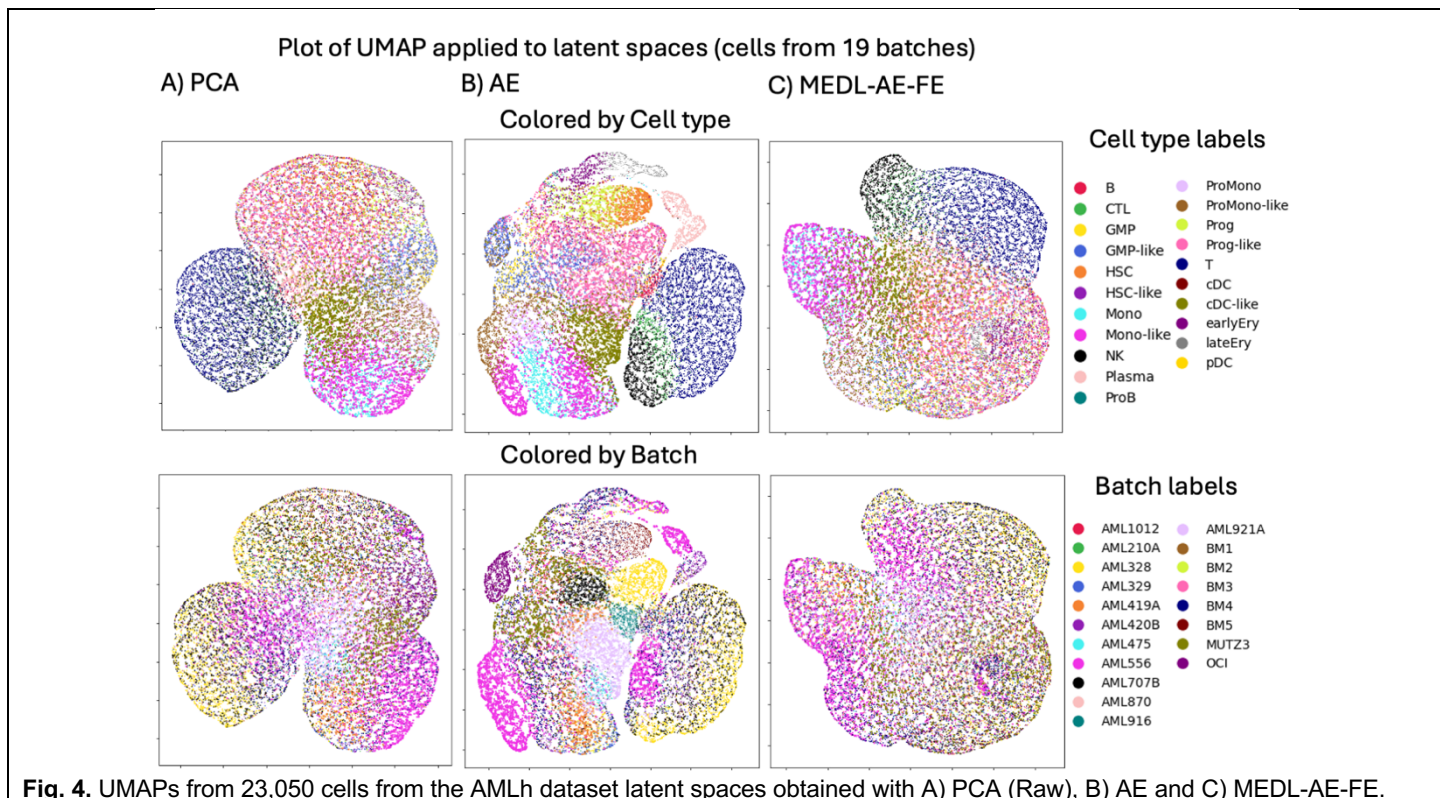
This reduction was attributable to the cell type–donor confounding factor; removing batch information led to the loss of some cell type information (Fig. 4B and 4C).

By comparing the latent spaces of the AE and MEDL-AE-FE models, it was observed that natural killer (NK), cytotoxic T lymphocyte (CTL), and T cells exhibited greater invariance to donor heterogeneity. Notably, these cell types lacked malignant counterparts, which explained their increased invariance in the MEDL-AE-FE representation compared to other cell types. This observation underscored the necessity of the MEDL-AE-RE model to recover donor variability that was removed by the MEDL-AE-FE.

Furthermore, the MEDL-AE-RE model effectively captured batch variability, as indicated by all ASW, 1/DB, and CH scores (Table 4 and Table S9). The MEDL-AE-RE latent space revealed that patients AML328 and AML556, as well as the cell line MUTZ3, exhibited greater heterogeneity compared to other patients and healthy donors

(Fig. S4). This distinction highlighted the model's ability to identify and separate highly heterogeneous batches, thereby enhancing our understanding of the underlying variability within the dataset.

The model with the strongest cell type signal was selected, prioritizing this signal over maximal batch correction (Table S6). This table presents the Average Silhouette Width (ASW) scores for both batch and cell type separability in the MEDL-AE-FE model, analyzed as a function of varying reconstruction loss weights. The results demonstrate that increasing the reconstruction loss weight enhances the mean cell type signal, indicating that prioritizing reconstruction loss (and thereby reducing the relative contribution of adversarial loss) favors retention of the cell type signal. This finding highlighted a trade-off between batch correction and preserving cell type signal, with the cell type–donor confounding factor likely contributing to this trade-off, where optimizing for batch correction could obscure cell type distinctions.



b) Assessment of the FE and RE subnetworks interpretability

The proposed approach offers novel capabilities for addressing "What if?" scenarios. For instance, how would a cell's gene expression profile change if the cell came from any other batch? What if it was originated from a donor with a different diagnosis, or from one with the same diagnosis? What if it came from a cell line? In the subsequent sections, the effectiveness of the method in answering such questions is demonstrated.

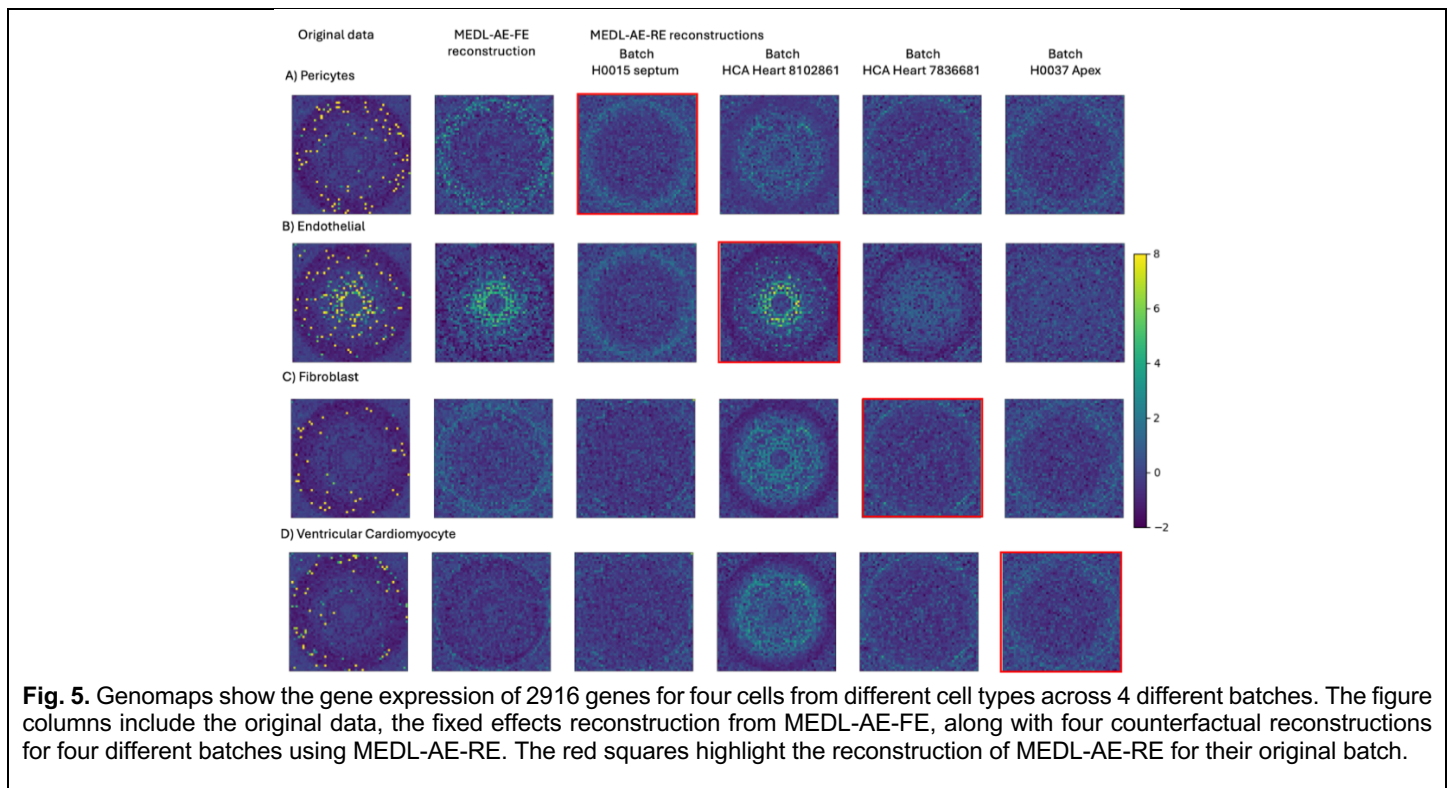
Healthy Heart Dataset

To demonstrate the effectiveness of the proposed method in modeling batch effects, four cell types from the Healthy Heart Dataset were selected to represent broad categories: pericytes, endothelial cells, fibroblasts, and ventricular cardiomyocytes. A random cell from each type was chosen, and its gene expression was visualized using a genomap (Fig. 5, first column). A genomap (Islam & Xing, 2023) displayed a cell's gene expression as an image, where each pixel represented a gene, and the pixel's intensity corresponded to the gene's scRNA-seq expression. The genes (pixels) were arranged in a polar plot, with genes exhibiting minimal gene-to-gene

interaction located at the center (the origin, with radius $\rho=0$), and those with progressively greater interaction positioned farther from the center (the angle θ was arbitrary).

In the first column, distinct genomap patterns were observed across the different cell types. The second column presented the genomap for the fixed effects reconstruction using the MEDL-AE-FE model, which captured the batch-independent characteristics of the cells. This visualization highlighted the variability between cell types, independent of batch effects.

In the remaining columns, the question was explored: What if the cells had come from a different batch? To address this, the cells were projected (reconstructed) as if they had originated from each of four different batches, including their own batch and three others (shown in columns three through six). Red square outlines indicated each cell's original batch. The MEDL-AE-RE model successfully learned batch-to-batch variability, as demonstrated by the visually distinct genomaps across each row for the same cell. Additionally, within each column, the variability between cell types remained apparent in the differing appearances of the genomaps. This illustrated that the model captured both cell type-specific and batch-specific patterns.

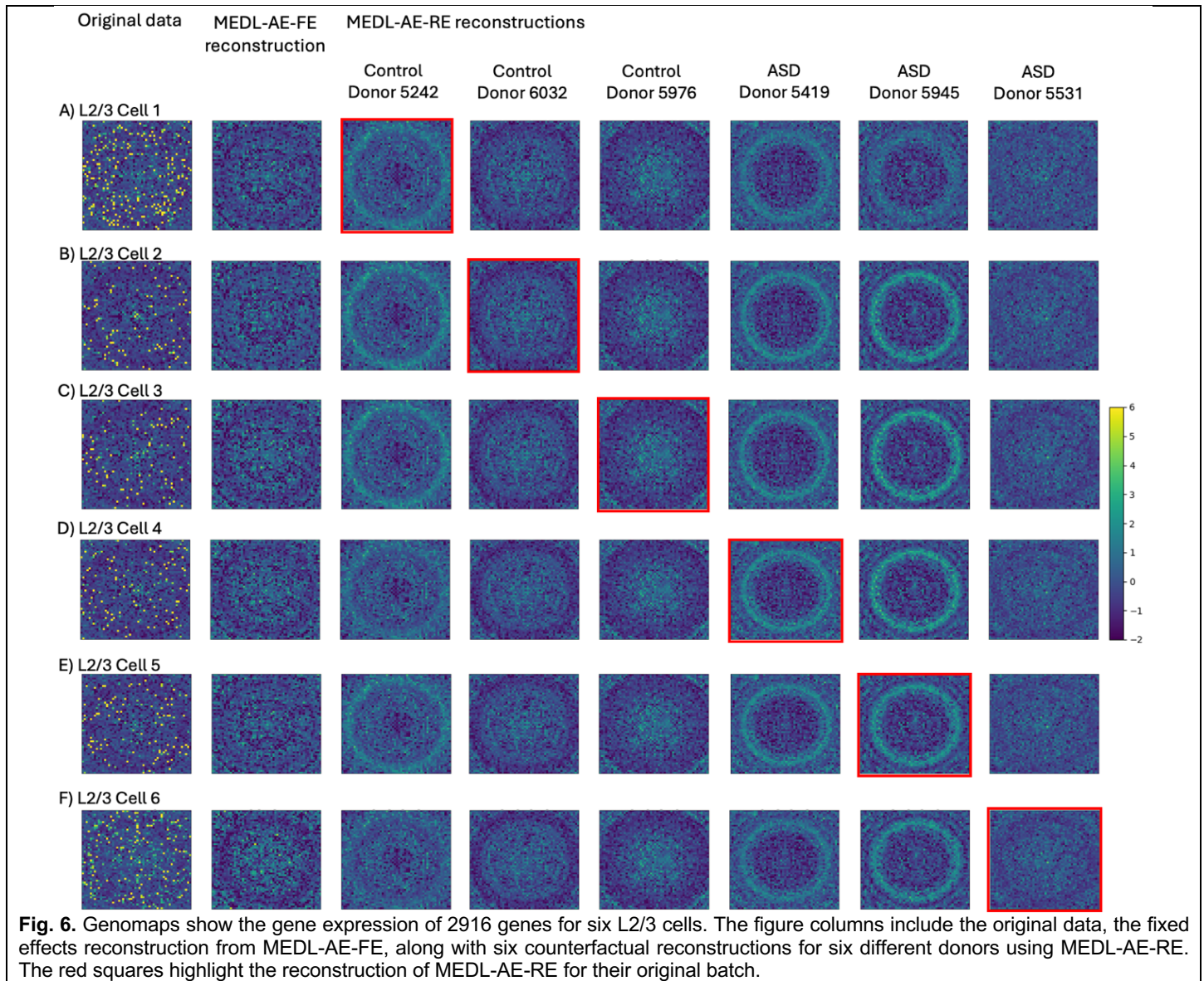


ASDc Dataset

In the ASDc dataset, donors were treated as batches to model donor-specific effects. Cells of the L2/3 neuronal subtype were selected, and their gene expression profiles were visualized using genomaps (Fig. 6, first column).

The first column revealed distinct genomap patterns between cells from control donors and those from autistic donors, highlighting differences in gene expression associated with autism. The second column displayed the fixed effects reconstruction using the MEDL-AE-FE model, capturing cell-type variability independent of donor effects.

To address the question of how a cell would appear if it had originated from a different donor—specifically, from a subject with autism versus a control—the cells were reconstructed as if they had come from each of several donors, including their own and others (shown in columns three through six). The MEDL-AE-RE model effectively captured donor-specific variability, as evidenced by the varying genomap patterns across each row for the same cell when projected onto different donors. Notably, cells projected onto autistic donors exhibited distinct gene expression patterns, such as more pronounced rings, compared to those projected onto control donors. The reconstruction corresponding to the original donor of each cell was highlighted in red. These findings demonstrated that the model captured both cell-type–specific and donor-specific patterns, enabling prediction of how gene expression might differ if a cell had come from a different donor.



AMLh Dataset

In the AMLh dataset, donors and cell lines were treated as batches. In the first column, distinct genomap patterns among normal and malignant monocytes from different healthy donors and cell lines were observed, highlighting natural variability between donors. The second column presented the fixed effects reconstruction using the MEDL-AE-FE model, which captured cell variability independent of the donor.

In the subsequent columns, the question was explored: How would a cell look if it had come from a different donor—specifically, from healthy donors, AML donors, or cell lines? To investigate this, both normal and malignant monocytes were reconstructed as if they had originated from various donors and cell lines (shown in columns three through six). The MEDL-AE-RE model effectively captured donor-specific and disease-specific variability, as evidenced by the varying genomap patterns across each row for the same cell.

Notably, gene expression patterns differed when normal cells were projected onto AML donors versus healthy donors, and vice versa for malignant cells. This demonstrated the model's ability to predict how gene expression would change if a cell were normal or malignant and had come from different donors or cell lines. The reconstruction corresponding to the original donor or cell line of each cell was highlighted in red.

Furthermore, the model revealed distinct gene expression patterns between healthy donors, AML donors, and cell lines. For instance, the MUTZ3 cell line exhibited high heterogeneity. This underscored the advantage of modeling random effects rather than merely suppressing them, allowing exploration of how gene expression varied between normal and malignant cells across different donors and batches.

This comprehensive modeling of both cell-type–specific and donor-specific patterns enhanced understanding of gene expression variability due to disease status and donor differences.

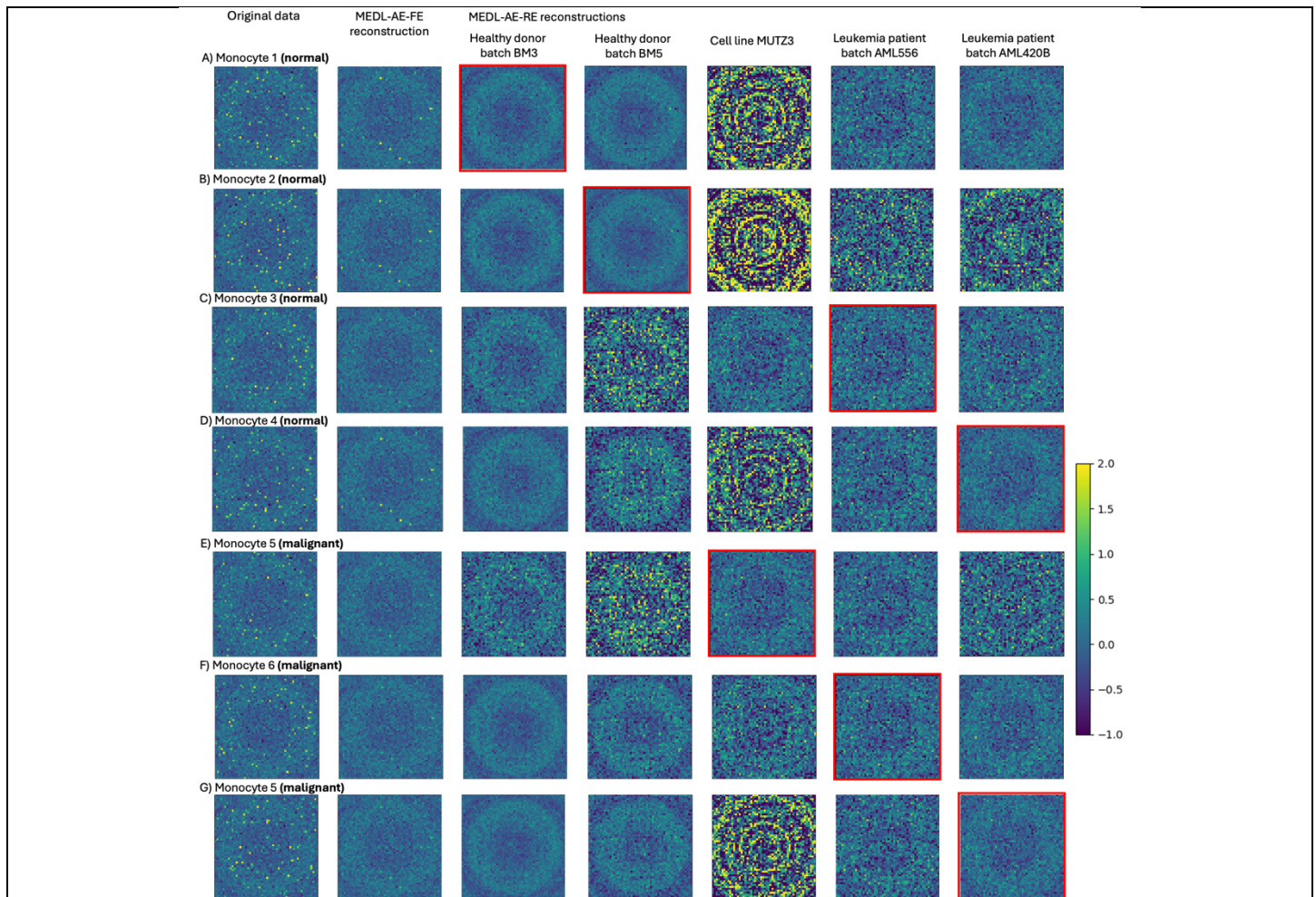


Fig. 7. Genomaps show gene expression level of 2916 genes for normal Monocytes (A-D) and malignant Monocytes (E-G) from different batches from 2 healthy donors, 2 leukemia patients (AML) and one cell type (MUTZ3). The figure columns include the original data, the fixed effects reconstruction from MEDL-AE-FE, along with five counterfactual reconstructions for four different batches using MEDL-AE-RE and one cell line. The red squares highlight the reconstruction of MEDL-AE-RE for their original batch.

4.1. Experiment 2. Evaluation of the complementary nature of the FE and RE latent representations for enhancing prediction performance

This experiment quantified the impact of a cell type classifier on batch and cell type separability by evaluating the complementary nature of fixed and random effects latent representations in enhancing prediction performance across various targets and databases.

Firstly, the aim was to determine whether cell type could be predicted more accurately using both latent spaces combined (fixed and random effects) than using either one alone, and whether this combination yielded better cell type classification than using either the PCA or AE latent spaces. When cell type was used as the target variable, the Random Forest classifier exhibited superior accuracy (ACC = 88.6%, 73.7%, and 60.4%) across all three datasets (Healthy Heart, ASDc, AMLh) when trained on latent spaces derived from both fixed and random effects (Table 5: first, second, and fourth rows). This performance surpassed that achieved when training on latent spaces derived solely from PCA (ACC = 70.8%, 49.1%, 43.4%) or fixed effects (ACC = 83.5%, 66.9%, 42.7%).

Table 5. Mean results across 5 folds and 95% confidence intervals (CI) obtained from the Random Forest Classifier applied to the Healthy Heart, ASDc, and AMLh datasets, with cell type as the primary target. In addition, the ASDc dataset includes diagnosis as a secondary target, and the AMLh Dataset includes patient group as a secondary target. The performance metrics reported include Accuracy, Balanced Accuracy, and Chance Accuracy.

Dataset	Target	Latent space	Accuracy			Balanced Accuracy			Chance Accuracy		
			mean	95%CI		mean	95%CI		mean	95%CI	
Healthy Heart (n = 486,134)	Cell types (k = 13)	PCA	70.8%	70.6%	70.9%	37.2%	37.0%	37.5%	16.2%	16.1%	16.3%
		MEDL-AE-FE	83.5%	82.2%	84.9%	57.4%	54.2%	60.6%			
		MEDL-AE (FE + RE)	88.6%	88.2%	88.9%	67.3%	65.1%	69.4%			
ASDc (n = 104,559)	Cell types (k = 17)	PCA	49.1%	48.6%	49.5%	38.1%	37.7%	38.6%	7.9%	7.8%	8.0%
		MEDL-AE-FE	66.9%	61.5%	72.2%	59.1%	52.0%	66.1%			
		MEDL-AE (FE + RE)	73.7%	69.8%	77.6%	67.0%	61.6%	72.4%			
	Diagnosis (k = 2)	PCA	52.8%	52.5%	53.2%	52.8%	52.5%	53.2%	50.1%	49.7%	50.4%
		MEDL-AE-FE MEDL-AE (FE + RE)	52.4%	52.0%	52.7%	52.4%	52.0%	52.7%			
AMLh (n = 38,417)	Cell types (k = 21)	PCA	43.4%	42.6%	44.2%	30.3%	29.5%	31.0%	8.0%	7.9%	8.1%
		MEDL-AE-FE	42.7%	40.7%	44.7%	30.0%	28.5%	31.6%			
		MEDL-AE (FE + RE)	60.4%	58.0%	62.8%	47.8%	45.1%	50.5%			
	Patient group (k = 3)	PCA	75.5%	75.1%	75.9%	51.2%	50.2%	52.3%	60.8%	60.4%	61.3%
		MEDL-AE-FE MEDL-AE (FE + RE)	72.0%	71.7%	72.4%	40.0%	38.6%	41.4%			

Secondly, the experiment sought to determine whether a different target could be predicted more accurately using both latent spaces. For the ASDc dataset, using diagnosis (typically developing versus autism spectrum disorder) as the target, the Random Forest classifier achieved the highest performance (ACC = 94.6%) when trained on latent spaces fusing (concatenating) both fixed and random effects. In contrast, classifiers trained on latent spaces derived from PCA or fixed effects alone barely exceeded chance accuracy, with ACCs of 52.8% and 52.4%, respectively. In the AMLh dataset, using patient group (healthy, AML, cell line) as the target variable, the Random Forest classifier trained on latent spaces fusing the fixed and random effects attained significantly

higher performance (ACC = 94.0%) compared to those derived from PCA or fixed effects alone, which attained ACCs of 75.5% and 72.0%, respectively.

These findings of superior accuracy in predicting cell type, diagnosis, and patient group targets underscored the efficacy of the proposed method, which simultaneously suppressed and quantified batch effects rather than merely suppressing them. The information extracted from each subnetwork was complementary.

Experiment 3. Quantification of the impact of a cell type classifier on batch and cell type separability

Healthy Heart dataset

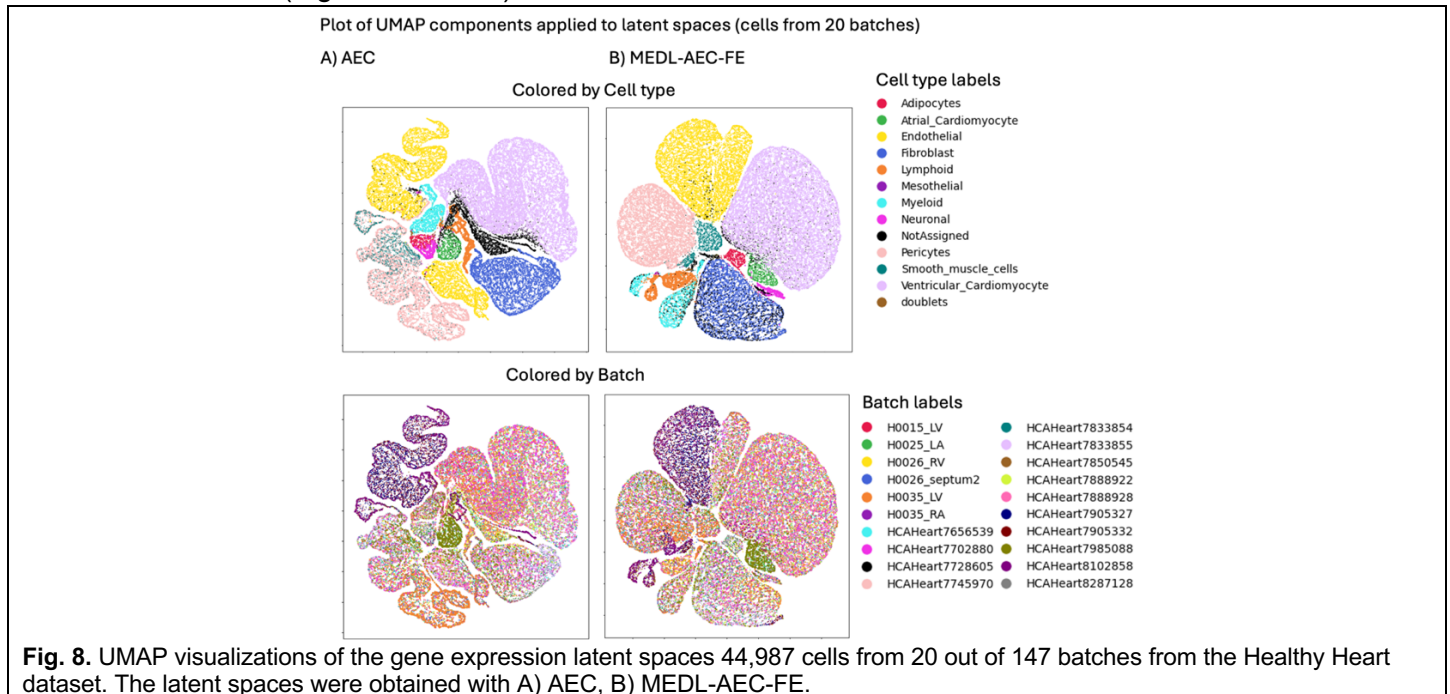
Integrating a cell type classifier into the base models—resulting in the AEC and MEDL-AEC-FE variants—led to improved mean ASW scores for both batch effects and cell type classification within the Healthy Heart dataset. Specifically, the mean ASW for cell type classification increased from 0.19 to 0.30 with the AEC, representing a 58% improvement. For the MEDL-AEC-FE model, this score increased from 0.16 to 0.28, reflecting a 75% improvement (Tables 2 and 6).

Although the ASW and CH clustering scores for batch and cell type suggested that the AEC outperformed MEDL-AEC-FE (Table 6 and S10), UMAP

	ASW (batch)			ASW (cell type)		
	mean	95% CI		mean	95% CI	
AEC	-0.59	-0.65	-0.54	0.30	0.25	0.36
MEDL-AEC-FE	-0.55	-0.57	-0.52	0.28	0.18	0.39

projections indicated that MEDL-AEC-FE better preserved the biological structure. The MEDL-AEC-FE latent space (Fig. 8B) more effectively maintained cell type biology than both the AEC (Fig. 8A) and MEDL-AE-FE models (Fig. 2C), and it reduced the number of cells within the 'Not Assigned' cluster compared to the AEC.

Including a cell type classifier in the AE model introduced false positives when cell type labels were uncertain. For instance, the AEC (Fig. 8A) displayed a significantly larger cluster of 'Not Assigned' cells compared to the AE and PCA models (Figs. 2A and 2C).



ASDc dataset

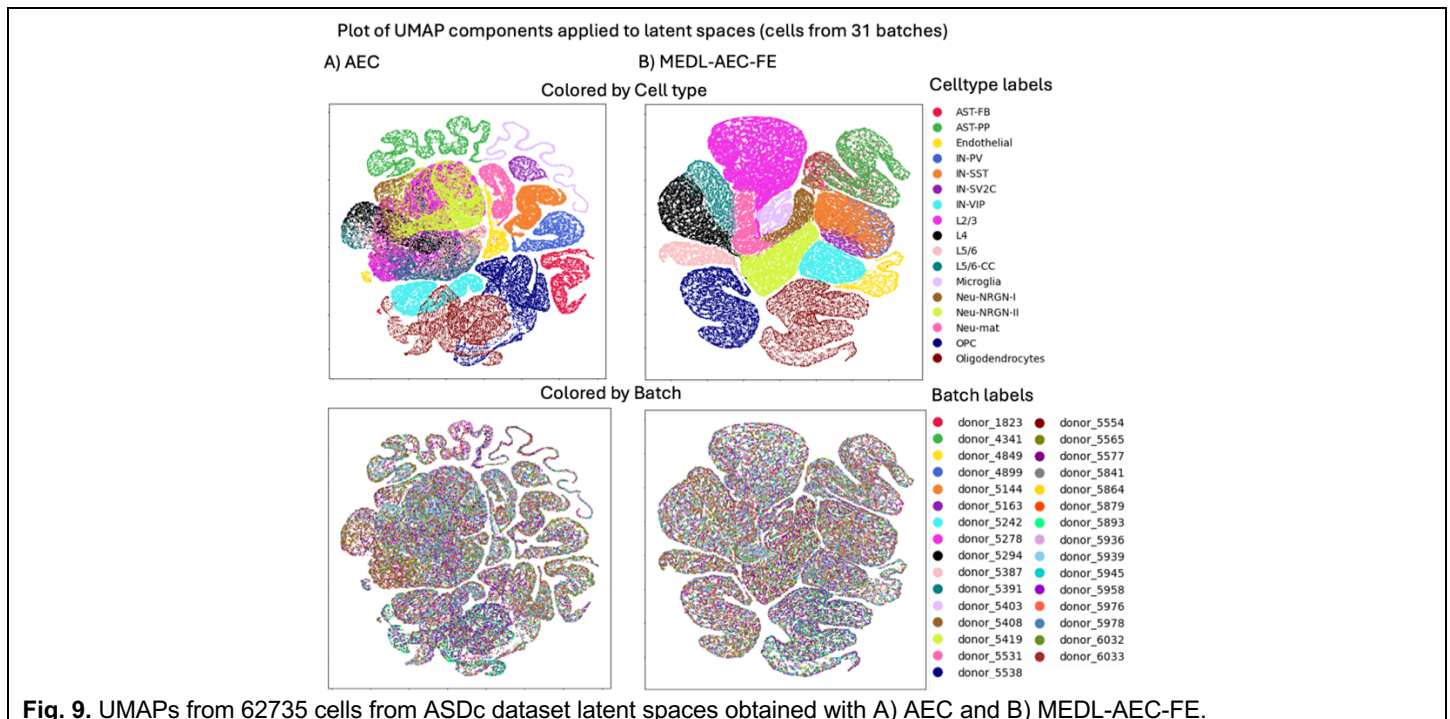
In the ASDc dataset, incorporating a classifier enhanced the MEDL-AE-FE model, increasing the mean cell type ASW score from 0.20 to 0.27, which represented a 35% improvement (Tables 3 and 7).

Although adding the classifier to the AEC model improved the performance of the AE, it did not preserve biological features as effectively as the AE alone, as illustrated in (Fig. 3B and 9A).

Table 7. Average Silhouette Width (ASW) scores (Mean and 95% CI across 5 folds) for batch and cell type separability in the latent spaces of the ASDc Heart Dataset, using AEC and MEDL-AEC-FE.

	ASW (batch)			ASW (cell type)		
	mean	95% CI		mean	95% CI	
AEC	-0.26	-0.30	-0.22	0.36	0.29	0.43
MEDL-AEC-FE	-0.22	-0.26	-0.19	0.27	0.21	0.33

Furthermore, while the AEC model achieved a higher overall score compared to the MEDL-AEC-FE model, the latter more effectively preserved biological characteristics (Fig. 9). Specifically, excitatory neurons (L cells) were more distinctly defined in the MEDL-AEC-FE model, and the boundaries between L cells and NeuN-NRGN (neurogranin-expressing) cells were more pronounced.



AMLh dataset

On this dataset, incorporating a classifier enhanced the cell type signal, whereas the adversarial component diminished it due to confounding between cell type and batch effects (Table S6).

Following the methodology employed in Experiment 1, the AEC and MEDL-AEC-FE models that maximized the cell type signal were selected. All relevant hyperparameters for this selection process are detailed in Table S6.

Table 8. Average Silhouette Width (ASW) scores (Mean and 95% CI across 5 folds) for batch and cell type separability in the latent spaces of the AMLh dataset, using AEC and MEDL-AEC-FE.

	ASW (batch)			ASW (cell type)		
	mean	95% CI		mean	95% CI	
AEC	-0.29	-0.34	-0.24	0.03	-0.04	0.10
MEDL-AEC-FE	-0.30	-0.37	-0.24	-0.05	-0.08	-0.02

In this dataset, which featured high-quality cell type labels, the AEC method preserved some of the cell type signal. Within the AEC latent space, clusters representing Monocytes (Mono), Progenitor cells (Prog), Hematopoietic Stem Cells (HSC), Granulocyte-Macrophage Progenitors (GMP), and Conventional Dendritic Cells (CDC) from both healthy cells and their malignant counterparts (designated with a "-like" suffix, such as Mono-like and Prog-like) were in proximity and, in some instances, overlapped (Fig. 10). This indicated that while the classifier effectively captured cell type-specific characteristics, it did not sufficiently distinguish between benign and malignant cells.

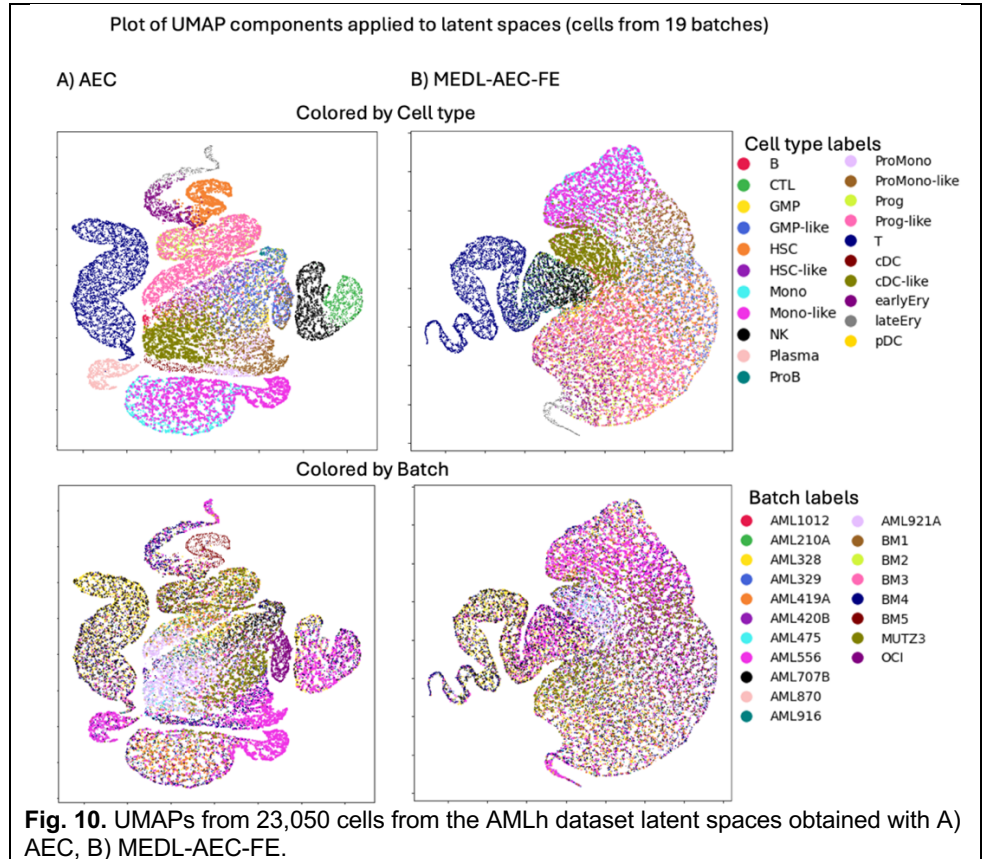


Fig. 10. UMAPs from 23,050 cells from the AMLh dataset latent spaces obtained with A) AEC, B) MEDL-AEC-FE.

Although the MEDL-AEC-FE method exhibited a superior ability to suppress batch effects (Table 8 and Fig. 10), this improvement compromised the clarity of the cell type signal. While the addition of the classifier restored some of the cell type signal, it was insufficient to fully resolve the confounding between cell type and donor information introduced by the adversarial component.

4. Discussion

We applied our MEDL framework to three datasets where batches contained valuable biological information, highlighting the benefits of modeling batch effects instead of discarding them. In Experiment 1, we found that using only the fixed-effects subnetwork led to a trade-off between suppressing batch effects and preserving cell type signals due to the choice of biologically informative batches. The random-effects subnetwork balanced this trade-off by capturing the information discarded by the fixed effects. This dual approach addresses two critical issues: mitigating loss of cell type information due to batch–cell type confounding and modeling batch effects valuable for describing donor heterogeneity.

Unlike other batch correction methods focusing on creating a batch-invariant space (e.g., iMAP, ResPAN, scDREAMER, IMAAE, ABC, DB-AAE), our MEDL framework explicitly learns batch distributions via the random-effects subnetwork. These methods do not include a random-effects subnetwork or explicitly model batch distributions. We demonstrated that learning batch distributions is necessary to recover information discarded by the fixed-effects subnetwork.

By comparing our fixed-effects subnetwork with the autoencoder, our approach enables introspective analysis of latent spaces, identifying cell types exhibiting the most heterogeneity across batches. In the Healthy Heart dataset, the fixed-effects subnetwork alone prevented misleading clustering of "not assigned" cell types seen in PCA and traditional autoencoder analyses, avoiding false clustering and incorrect cell type annotation.

The 2D visualizations of individual cells revealed variability across batches and cell types: differences between autism and control donors, and between malignant and normal cells from healthy, AML patients and cell lines in the AMLh dataset. Our model's ability to present a consistent visualization of a cell across different batches represents a significant advancement in personalized single-cell modeling. Unlike AIF model that incorporates batch modeling without explicitly separating batch effects, our approach offers enhanced explainability by isolating batch variability, facilitating the disentanglement of batch effects from other variations.

Our approach is novel in using batch projections to answer "what if" questions. We are the first ones to exploit cell projections for hypothetical scenarios or separate fixed and random effects in scRNA-Seq data with a deep learning method. This enhances the explainability of our model compared to existing methods.

Traditionally, batch correction evaluation focuses on clustering metrics (Buttner et al., 2019; Haghverdi et al., 2018; Luecken & Theis, 2019; Tran et al., 2020) rather than classification performance. A complementary integration of FE and RE latent spaces improved classification accuracy of both cell type and diagnoses. This demonstrates the practical utility of leveraging batch effects information. The combined model outperformed both PCA and the fixed-effects subnetwork alone in classification performance across all tested targets and datasets. This supports the findings of Experiment 1: while the fixed-effects subnetwork discards essential batch-related variability, the random-effects subnetwork captures this variability, leading to more robust and comprehensive modeling of scRNA-seq data.

To preserve the cell type biology within the batch-invariant space, we examined incorporating a cell type classifier into the MEDL-AE-FE subnetwork. Methods like AutoClass (Li et al., 2020), scDREAMER (Shree et al., 2023), and ABC (Danino et al., 2024) incorporate cell type classifiers in their supervised approaches for batch effect suppression and cell type biology preservation. As shown in scDREAMER's ablation tests, the cell type classifier effectively enhances cell type separability. However, using a cell type classifier requires available cell type labels, which may involve prior annotation prone to human error. Utilizing low-quality or undefined labels can lead to false clustering and incorrect biological interpretations, as we identified in the AEC but mitigated with our MEDL-AEC-FE. We underscore the importance of high-quality labels when adding a cell type classifier for biology preservation. Simple autoencoder models with a cell type classifier like AutoClass do not adequately prevent false positives from mislabeled datasets, potentially leading to erroneous conclusions.

The AMLh dataset presented unique challenges due to a substantial confound between cell type and batch effect (donor), as certain cell types were present only in specific donors. In such datasets, maintaining the cell type signal is challenging even with a cell type classifier in the fixed-effects subnetwork. This highlights the necessity of effectively modeling batch variability to recover information discarded by batch suppression methods.

In summary, we propose a general framework for batch effect suppression and modeling. The fixed-effects subnetwork we used is just one example; our framework supports independent training of both fixed (batch effect suppression) and random-effects subnetworks. This flexibility allows the integration of other batch-invariant models alongside the proposed MEDL-AE-RE model, potentially enhancing performance and interpretability in scRNA-seq analysis

5. Limitations

Our scRNA-seq MEDL subnetworks used a latent space of dimensions $(n, 2)$ with n cells and a bottleneck dimension of 2. We leave for future work to assess performance in higher-dimensional latent spaces.

Showing how our random-effects subnetwork complements other batch suppression methods remains for future work. This study explores a mixed-effects deep learning framework to both suppress and model batch effects, which has the potential to complement existing methods focused solely on suppression. Our flexible framework reveals new capabilities for addressing biological questions—a capacity traditional batch suppression methods lack.

The framework requires hyperparameter optimization, particularly the weights assigned to loss functions in the fixed and random-effects subnetworks. Factors like the number of batches and cell types must be considered to adjust these weights, ensuring all loss functions are on a similar scale. For instance, with more classes, each class's contribution to the total loss diminishes, which can be addressed by tuning the weights of each individual loss function.

Finally, although we tested on diverse datasets covering various diseases and body regions, our evaluation is not exhaustive. A comprehensive assessment is beyond the scope of this initial demonstration.

6. Conclusions

In this study, we introduced a mixed effects deep learning (MEDL) method for single-cell RNA sequencing (scRNA-seq) data analysis, offering a novel approach that quantitatively and separately models fixed and random effects. Our key contributions are: 1) the development of a novel MEDL framework that, to our knowledge, is the first in scRNA-seq analysis to separately model fixed effects (batch-invariant biological signals) and random effects (batch-specific variability), 2) demonstrating that this framework effectively suppresses batch effects through the fixed effects subnetwork, creating a batch-invariant latent space, while the random effects subnetwork captures batch-specific variability, thereby enhancing accuracy and interpretability, 3) exploring 'what-if' analyses by leveraging the modeled batch effects—such as predicting a cell's expression profile if it originated from a different batch or diseased subject—exemplified through genomap visualizations revealing subtypes in and ASDc dataset and donor and cell line variability in AMLh dataset, 4) achieving significant improvements in classification accuracy by combining the fixed (batch-agnostic) and random (batch-representative) effects representations, suggesting that retaining batch variability alongside batch invariance enhances performance, 5) preventing false clustering observed in PCA, autoencoders, and autoencoders with a cell type classifier when using low-quality labels, 6) preserving cell type biology in the latent space through the addition of a cell type classifier to the fixed effects subnetwork. Demonstrated across diverse scRNA-seq datasets encompassing various health conditions, cell types, and batch effects, our method underscores the necessity of both fixed and random effects latent spaces for comprehensive modeling.

7. Data and code availability

Upon acceptance of this publication in a journal, all code for this paper including interpretable scRNA-seq analysis, ablation tests and reproducibility scripts, will be released on GitHub: <https://github.com/DeepLearningForPrecisionHealthLab/MEDLforRNAseqData>.

Gene expression matrices and cell annotations for the AMLh dataset were obtained from the Gene Expression Omnibus (GEO) under accession number [GSE116256](https://www.ncbi.nlm.nih.gov/geo/query/acc.cgi?acc=GSE116256) (van Galen et al., 2019). The Healthy Heart dataset was acquired from Yu et al. (2023) via figshare (DOI: <https://doi.org/10.6084/m9.figshare.20499630.v2>) (Yu et al., 2023b), though they also reference the Heart Cell Atlas (<https://www.heartcellatlas.org/>) (Litvinukova et al., 2020). The log₂-transformed ASDc dataset was downloaded from the UCSC Cell Browser (<https://autism.cells.ucsc.edu>) (Speir et al., 2021; Velmeshev et al., 2019b)

8. Acknowledgements

This study was supported by the NIH R01 Grant (5R01GM144486-02), titled “Correcting Biases in Deep Learning Models.” We also acknowledge the BioHPC supercomputing facility at the Lyda Hill Department of Bioinformatics, UT Southwestern Medical Center, TX, for providing computational resources (URL: <https://portal.biohpc.swmed.edu>). Special thanks to Dr. Prapti Mody for her invaluable feedback on this work.

9. References

- Blei, D. M., Kucukelbir, A., & McAuliffe, J. D. (2017). Variational Inference: A Review for Statisticians. *Journal of the American Statistical Association*, 112(518), 859-877. <https://doi.org/10.1080/01621459.2017.1285773>
- Bouland, G. A., Mahfouz, A., & Reinders, M. J. T. (2023). Consequences and opportunities arising due to sparser single-cell RNA-seq datasets. *Genome Biol*, 24(1), 86. <https://doi.org/10.1186/s13059-023-02933-w>
- Breiman, L. (2001). *Machine Learning*, 45(1), 5-32. <https://doi.org/10.1023/a:1010933404324>
- Buttner, M., Miao, Z., Wolf, F. A., Teichmann, S. A., & Theis, F. J. (2019). A test metric for assessing single-cell RNA-seq batch correction. *Nat Methods*, 16(1), 43-49. <https://doi.org/10.1038/s41592-018-0254-1>
- Calinski, T., & Harabasz, J. (1974). A dendrite method for cluster analysis. *Communications in Statistics - Theory and Methods*, 3(1), 1-27. <https://doi.org/10.1080/03610927408827101>
- Dai, C., Chen, M., Wang, C., & Hao, X. (2021). Deconvolution of Bulk Gene Expression Profiles with Single-Cell Transcriptomics to Develop a Cell Type Composition-Based Prognostic Model for Acute Myeloid Leukemia. *Front Cell Dev Biol*, 9, 762260. <https://doi.org/10.3389/fcell.2021.762260>
- Danino, R., Nachman, I., & Sharan, R. (2024). Batch correction of single-cell sequencing data via an autoencoder architecture. *Bioinform Adv*, 4(1), vbad186. <https://doi.org/10.1093/bioadv/vbad186>
- Davies, D. L., & Bouldin, D. W. (1979). A Cluster Separation Measure. *IEEE Transactions on Pattern Analysis and Machine Intelligence*, PAMI-1(2), 224-227. <https://doi.org/10.1109/tpami.1979.4766909>
- Gronbeck, C. H., Vording, M. F., Timshel, P. N., Sonderby, C. K., Pers, T. H., & Winther, O. (2020). scVAE: variational auto-encoders for single-cell gene expression data. *Bioinformatics*, 36(16), 4415-4422. <https://doi.org/10.1093/bioinformatics/btaa293>
- Haghverdi, L., Lun, A. T. L., Morgan, M. D., & Marioni, J. C. (2018). Batch effects in single-cell RNA-sequencing data are corrected by matching mutual nearest neighbors. *Nat Biotechnol*, 36(5), 421-427. <https://doi.org/10.1038/nbt.4091>
- Hu, Y., Xie, M., Li, Y., Rao, M., Shen, W., Luo, C., Qin, H., Baek, J., & Zhou, X. M. (2024). Benchmarking clustering, alignment, and integration methods for spatial transcriptomics. *Genome Biol*, 25(1), 212. <https://doi.org/10.1186/s13059-024-03361-0>
- Hwang, B., Lee, J. H., & Bang, D. (2018). Single-cell RNA sequencing technologies and bioinformatics pipelines. *Exp Mol Med*, 50(8), 1-14. <https://doi.org/10.1038/s12276-018-0071-8>

- Hwang, H., Jeon, H., Yeo, N., & Baek, D. (2024). Big data and deep learning for RNA biology. *Exp Mol Med*, 56(6), 1293-1321. <https://doi.org/10.1038/s12276-024-01243-w>
- Islam, M. T., & Xing, L. (2023). Cartography of Genomic Interactions Enables Deep Analysis of Single-Cell Expression Data. *Nat Commun*, 14(1), 679. <https://doi.org/10.1038/s41467-023-36383-6>
- Ko, K. D., & Sartorelli, V. (2024). A deep learning adversarial autoencoder with dynamic batching displays high performance in denoising and ordering scRNA-seq data. *iScience*, 27(3), 109027. <https://doi.org/10.1016/j.isci.2024.109027>
- Li, H., Brouwer, C. R., & Luo, W. (2022). A universal deep neural network for in-depth cleaning of single-cell RNA-Seq data. *Nat Commun*, 13(1), 1901. <https://doi.org/10.1038/s41467-022-29576-y>
- Li, X., Wang, K., Lyu, Y., Pan, H., Zhang, J., Stambolian, D., Susztak, K., Reilly, M. P., Hu, G., & Li, M. (2020). Deep learning enables accurate clustering with batch effect removal in single-cell RNA-seq analysis. *Nat Commun*, 11(1), 2338. <https://doi.org/10.1038/s41467-020-15851-3>
- Li, X., Zhang, S., & Wong, K. C. (2021). Deep embedded clustering with multiple objectives on scRNA-seq data. *Brief Bioinform*, 22(5). <https://doi.org/10.1093/bib/bbab090>
- Litvinukova, M., Talavera-Lopez, C., Maatz, H., Reichart, D., Worth, C. L., Lindberg, E. L., Kanda, M., Polanski, K., Heinig, M., Lee, M., Nadelmann, E. R., Roberts, K., Tuck, L., Fasouli, E. S., DeLaughter, D. M., McDonough, B., Wakimoto, H., Gorham, J. M., Samari, S.,...Teichmann, S. A. (2020). Cells of the adult human heart. *Nature*, 588(7838), 466-472. <https://doi.org/10.1038/s41586-020-2797-4>
- Luecken, M. D., Buttner, M., Chaichoompu, K., Danese, A., Interlandi, M., Mueller, M. F., Strobl, D. C., Zappia, L., Dugas, M., Colome-Tatche, M., & Theis, F. J. (2022). Benchmarking atlas-level data integration in single-cell genomics. *Nat Methods*, 19(1), 41-50. <https://doi.org/10.1038/s41592-021-01336-8>
- Luecken, M. D., & Theis, F. J. (2019). Current best practices in single-cell RNA-seq analysis: a tutorial. *Mol Syst Biol*, 15(6), e8746. <https://doi.org/10.15252/msb.20188746>
- Martín Abadi, A. A., Paul Barham, Eugene Brevdo,, Zhifeng Chen, C. C., Greg S. Corrado, Andy Davis,, Jeffrey Dean, M. D., Sanjay Ghemawat, Ian Goodfellow,, Andrew Harp, G. I., Michael Isard, Rafal Jozefowicz, Yangqing Jia,, Lukasz Kaiser, M. K., Josh Levenberg, Dan Mané, Mike Schuster,, Rajat Monga, S. M., Derek Murray, Chris Olah, Jonathon Shlens,, Benoit Steiner, I. S., Kunal Talwar, Paul Tucker,, Vincent Vanhoucke, V. V., Fernanda Viégas,, Oriol Vinyals, P. W., Martin Wattenberg, Martin Wicke,, & Yuan Yu, a. X. Z. (2015). TensorFlow: Large-scale machine learning on heterogeneous systems. *White Paper*. <https://doi.org/10.5281/zenodo.4724125>
- McInnes, L., Healy, J., & Melville, J. (2018). Umap: uniform manifold approximation and projection for dimension reduction. *arXiv*. <https://doi.org/10.48550/ARXIV.1802.03426>
- Monnier, L., & Cournede, P. H. (2024). A novel batch-effect correction method for scRNA-seq data based on Adversarial Information Factorization. *PLoS Comput Biol*, 20(2), e1011880. <https://doi.org/10.1371/journal.pcbi.1011880>
- Nguyen, K. P., Treacher, A. H., & Montillo, A. A. (2023). Adversarially-Regularized Mixed Effects Deep Learning (ARMED) Models Improve Interpretability, Performance, and Generalization on Clustered (non-iid) Data. *IEEE Trans Pattern Anal Mach Intell*, 45(7), 8081-8093. <https://doi.org/10.1109/TPAMI.2023.3234291>
- Ning, Z., Dai, Z., Zhang, H., Chen, Y., & Yuan, Z. (2023). A clustering method for small scRNA-seq data based on subspace and weighted distance. *PeerJ*, 11, e14706. <https://doi.org/10.7717/peerj.14706>
- Pedregosa, F., Eickenberg, M., Ciuciu, P., Thirion, B., & Gramfort, A. (2015). Data-driven HRF estimation for encoding and decoding models. *Neuroimage*, 104, 209-220. <https://doi.org/10.1016/j.neuroimage.2014.09.060>
- Rousseeuw, P. J. (1987). Silhouettes: A graphical aid to the interpretation and validation of cluster analysis. *Journal of Computational and Applied Mathematics*, 20, 53-65. [https://doi.org/10.1016/0377-0427\(87\)90125-7](https://doi.org/10.1016/0377-0427(87)90125-7)
- Shree, A., Pavan, M. K., & Zafar, H. (2023). scDREAMER for atlas-level integration of single-cell datasets using deep generative model paired with adversarial classifier. *Nat Commun*, 14(1), 7781. <https://doi.org/10.1038/s41467-023-43590-8>
- Speir, M. L., Bhaduri, A., Markov, N. S., Moreno, P., Nowakowski, T. J., Papatheodorou, I., Pollen, A. A., Raney, B. J., Seninge, L., Kent, W. J., & Haeussler, M. (2021). UCSC Cell Browser: visualize your single-cell data. *Bioinformatics*, 37(23), 4578-4580. <https://doi.org/10.1093/bioinformatics/btab503>

- Tran, H. T. N., Ang, K. S., Chevrier, M., Zhang, X., Lee, N. Y. S., Goh, M., & Chen, J. (2020). A benchmark of batch-effect correction methods for single-cell RNA sequencing data. *Genome Biol*, 21(1), 12. <https://doi.org/10.1186/s13059-019-1850-9>
- Tung, P. Y., Blischak, J. D., Hsiao, C. J., Knowles, D. A., Burnett, J. E., Pritchard, J. K., & Gilad, Y. (2017). Batch effects and the effective design of single-cell gene expression studies. *Sci Rep*, 7, 39921. <https://doi.org/10.1038/srep39921>
- van Galen, P., Hovestadt, V., Wadsworth li, M. H., Hughes, T. K., Griffin, G. K., Battaglia, S., Verga, J. A., Stephansky, J., Pastika, T. J., Lombardi Story, J., Pinkus, G. S., Pozdnyakova, O., Galinsky, I., Stone, R. M., Graubert, T. A., Shalek, A. K., Aster, J. C., Lane, A. A., & Bernstein, B. E. (2019). Single-Cell RNA-Seq Reveals AML Hierarchies Relevant to Disease Progression and Immunity. *Cell*, 176(6), 1265-1281 e1224. <https://doi.org/10.1016/j.cell.2019.01.031>
- Velmeshev, D., Schirmer, L., Jung, D., Haeussler, M., Perez, Y., Mayer, S., Bhaduri, A., Goyal, N., Rowitch, D. H., & Kriegstein, A. R. (2019a). *Single-cell genomics identifies cell type-specific molecular changes in autism* (<https://autism.cells.ucsc.edu>)
- Velmeshev, D., Schirmer, L., Jung, D., Haeussler, M., Perez, Y., Mayer, S., Bhaduri, A., Goyal, N., Rowitch, D. H., & Kriegstein, A. R. (2019b). Single-cell genomics identifies cell type-specific molecular changes in autism. *Science*, 364(6441), 685-689. <https://doi.org/10.1126/science.aav8130>
- Vendramin, L., Campello, R. J. G. B., & Hruschka, E. R. (2010). Relative clustering validity criteria: A comparative overview. *Statistical Analysis and Data Mining: The ASA Data Science Journal*, 3(4), 209-235. <https://doi.org/10.1002/sam.10080>
- Vestal, B. E., Wynn, E., & Moore, C. M. (2022). ImerSeq: an R package for analyzing transformed RNA-Seq data with linear mixed effects models. *BMC Bioinformatics*, 23(1), 489. <https://doi.org/10.1186/s12859-022-05019-9>
- Wang, D., Hou, S., Zhang, L., Wang, X., Liu, B., & Zhang, Z. (2021). iMAP: integration of multiple single-cell datasets by adversarial paired transfer networks. *Genome Biol*, 22(1), 63. <https://doi.org/10.1186/s13059-021-02280-8>
- Wang, L., Hong, C., Song, J., & Yao, J. (2024). CTEC: a cross-tabulation ensemble clustering approach for single-cell RNA sequencing data analysis. *Bioinformatics*, 40(4). <https://doi.org/10.1093/bioinformatics/btae130>
- Wang, T., Johnson, T. S., Shao, W., Lu, Z., Helm, B. R., Zhang, J., & Huang, K. (2019). BERMUDA: a novel deep transfer learning method for single-cell RNA sequencing batch correction reveals hidden high-resolution cellular subtypes. *Genome Biol*, 20(1), 165. <https://doi.org/10.1186/s13059-019-1764-6>
- Wang, X., Zhang, C., Wang, L., & Zheng, P. (2023). Integrating Multiple Single-Cell RNA Sequencing Datasets Using Adversarial Autoencoders. *Int J Mol Sci*, 24(6). <https://doi.org/10.3390/ijms24065502>
- Wang, Y., Liu, T., & Zhao, H. (2022). ResPAN: a powerful batch correction model for scRNA-seq data through residual adversarial networks. *Bioinformatics*, 38(16), 3942-3949. <https://doi.org/10.1093/bioinformatics/btac427>
- Wolf, F. A., Angerer, P., & Theis, F. J. (2018). SCANPY: large-scale single-cell gene expression data analysis. *Genome Biol*, 19(1), 15. <https://doi.org/10.1186/s13059-017-1382-0>
- Wu, Y., & Zhang, K. (2020). Tools for the analysis of high-dimensional single-cell RNA sequencing data. *Nat Rev Nephrol*, 16(7), 408-421. <https://doi.org/10.1038/s41581-020-0262-0>
- Yousuff, M., Babu, R., & Rathinam, A. (2024). Nonlinear dimensionality reduction based visualization of single-cell RNA sequencing data. *Journal of Analytical Science and Technology*, 15(1). <https://doi.org/10.1186/s40543-023-00414-0>
- Yu, L., Cao, Y., Yang, J. Y. H., & Yang, P. (2022). Benchmarking clustering algorithms on estimating the number of cell types from single-cell RNA-sequencing data. *Genome Biol*, 23(1), 49. <https://doi.org/10.1186/s13059-022-02622-0>
- Yu, X., Xu, X., Zhang, J., & Li, X. (2023a). Batch alignment of single-cell transcriptomics data using deep metric learning. *Nat Commun*, 14(1), 960. <https://doi.org/10.1038/s41467-023-36635-5>
- Yu, X., Xu, X., Zhang, J., & Li, X. (2023b). Batch alignment of single-cell transcriptomics data using deep metric learning. *figshare*. <https://doi.org/https://doi.org/10.6084/m9.figshare.20499630.v2>

Mixed Effects Deep Learning Autoencoder for interpretable analysis of single cell RNA Sequencing data

Supplemental

<i>Supplemental Methods</i>	2
Hyperparameters used on the AE, AEC, MEDL-AE-FE, MEDL-AEC-FE, and MEDL-AE-RE models	2
Data Preprocessing pipeline	5
UMAP Visualization parameters	5
Hardware	5
<i>Supplemental Results</i>	6
Supplementary Figures for Dataset Description	6
Donor Representation Across Cell Types in AMLh dataset	6
Hyperparameter Optimization for Experiments 1 A) and 3	7
ASW Scores for Batch and Cell Type Separability	7
Supplementary Results for Experiment 1 A)	8
CH and 1/DB scores	8
Random Effects Subnetwork (MEDL-AE-RE) latent spaces	9
Average Training and Validation Curves for AE, MEDL-AE-FE, and MEDL-AE-RE Across 5 Folds in the Healthy Heart, ASDc, and AMLh Datasets	11
Supplementary Results for Experiment 3	14
CH and 1/DB scores	14
Average Training and Validation Curves for AEC and MEDL-AEC-FE Across 5 Folds in the Healthy Heart, ASDc, and AMLh Datasets	15
<i>References</i>	17

Supplemental Methods

Hyperparameters used on the AE, AEC, MEDL-AE-FE, MEDL-AEC-FE, and MEDL-AE-RE models

In Table S1-S3 there are described the Hyperparameters for data loading, model construction, compilation, and training were applied across the AE, AEC, MEDL-AE-FE, MEDL-AEC-FE, and MEDL-AE-RE models in three datasets: Healthy Heart, the Autism Spectrum Disorder (ASD) and control (ASDc) dataset, and Acute Myeloid Leukemia (AML) and healthy (AMLh).

Table S1. Hyperparameters and parameters for data loading, model building, compilation, and training in the Healthy Heart Dataset.

Settings	Hyperparameter/Parameter	AE	AEC	MEDL-AE-FE	MEDL-AEC-FE	MEDL-AE-RE
Compile model	optimizer 1	Adam(lr=0.0001)				
	optimizer 2 (adversarial)	-	-	Adam(lr=0.0001)	Adam(lr=0.0001)	-
	reconstruction loss (X)	MSE				
	adversarial loss (z)	-	-	CCE	CCE	-
	classification loss (y)	-	CCE	-	CCE	-
	classification loss (z)	-	-	-	-	CCE
	reconstruction loss_weights (X)	1	81	5400	9450	110
	classification loss_weights (y)	-	0.1	-	1	-
	adversarial loss weights (z)	-	-	1	1	-
	cluster loss weight (z)					0.1
Build model	kl_weight (z)					1.00E-05
	post_loc_init_scale (z)					0.1
	prior_scale (z)					0.25
	n_latent_dims	2				
	layer_units	[512,132]				
	layer_units_latent_classifier	-	[2]	-	[2]	[5]
	n_clusters	-	-	147	147	147
	n_pred (y)	-	13	-	13	-
	last_activation	linear				
	use_batch_norm	TRUE				default in RE layers
	dense hidden layers activation	selu				
	classifier activation	softmax				
Load data	use_z	FALSE	FALSE	TRUE	TRUE	TRUE
	get_pred (y)	FALSE	TRUE	FALSE	TRUE	FALSE
	scaling	min_max				
	batch_size	512				
Train model	epochs	500				
	monitor_metric	val_loss	val_loss	val_total_loss	val_total_loss	val_total_loss
	patience	30				
	stop_criteria	early_stopping				

Table S2. Hyperparameters and parameters for data loading, model building, compilation, and training in the ASDc Dataset.

Settings	Hyperparameter/Parameter	AE	AEC	MEDL-AE-FE	MEDL-AEC-FE	MEDL-AE-RE
Compile model	optimizer 1	Adam(lr=0.0001)				
	optimizer 2 (adversarial)	-	-	Adam(lr=0.0001)	Adam(lr=0.0001)	-
	reconstruction loss (X)	MSE				
	adversarial loss (z)	-	-	CCE	CCE	-
	classification loss (y)	-	CCE	-	CCE	-
	classification loss (z)	-	-	-	-	CCE
	reconstruction loss_weights (X)	1	1	1000	1000	110
	classification loss_weights (y)	-	0.1	-	1	-
	adversarial loss weights (z)	-	-	1	1	-
	cluster loss weight (z)					0.1
Build model	kl_weight (z)					1.00E-05
	post_loc_init_scale (z)					0.1
	prior_scale (z)					0.25
	n_latent_dims	2				
	layer_units	[512,132]				
	layer_units_latent_classifier	NA	[2]	-	[2]	[5]
	n_clusters	-	-	31	31	31
	n_pred (y)	NA	17	-	17	17
	last_activation	linear				
	use_batch_norm	TRUE				default in RE layers
	dense hidden layers activation	selu				
	classifier activation	softmax				
Load data	use_z	FALSE	FALSE	TRUE	TRUE	TRUE
	get_pred (y)	FALSE	TRUE	FALSE	TRUE	FALSE
	scaling	min_max				
	batch_size	512				
Train model	epochs	500				
	monitor_metric	val_loss	val_loss	val_total_loss	val_total_loss	val_total_loss
	patience	30				
	stop_criteria	early_stopping				

Table S3. Hyperparameters and parameters for data loading, model building, compilation, and training in the AMLh Dataset.

Settings	Hyperparameter/Parameter	AE	AEC	MEDL-AE-FE	MEDL-AEC-FE	MEDL-AE-RE	
Compile model	optimizer 1	Adam(lr=0.0001)					
	optimizer 2 (adversarial)	-	-	Adam(lr=0.0001)	Adam(lr=0.0001)	-	
	reconstruction loss (X)	MSE					
	adversarial loss (z)	-	-	CCE	CCE	-	
	classification loss (y)	-	CCE	-	CCE	-	
	classification loss (z)	-	-	-	-	CCE	
	reconstruction loss_weights (X)	1	100	4000	1500	110	
	classification loss_weights (y)	-	0.1	-	1	-	
	adversarial loss weights (z)	-	-	1	1	-	
	cluster loss weight (z)	-					0.1
Build model	kl_weight (z)	-					1.00E-05
	post_loc_init_scale (z)	-					0.1
	prior_scale (z)	-					0.25
	n_latent_dims	2					
	layer_units	[512,132]					
	layer_units_latent_classifier	-	[2]	-	[2]	[5]	
	n_clusters	-	-	19	19	19	
	n_pred (y)	-	21	-	21	-	
	last_activation	linear					
	use_batch_norm	TRUE					default in RE layers
	dense hidden layers activation	selu					
	classifier activation	softmax					
Load data	use_z	FALSE	FALSE	TRUE	TRUE	TRUE	
	get_pred (y)	FALSE	TRUE	FALSE	TRUE	FALSE	
	scaling	min_max					
	batch_size	512					
Train model	epochs	500					
	monitor_metric	val_loss	val_loss	val_total_loss	val_total_loss	val_total_loss	
	patience	30					
	stop_criteria	early_stopping					

Data Preprocessing pipeline

We used standard preprocessing steps from Yu et al. , 2023 (Yu et al., 2023): 1) filtering out cells exhibiting expression in fewer than ten genes and removed genes detected in fewer than three cells, 2) normalizing total Unique molecular identifiers (UMI) counts per cell to 10,000, 3) log-transforming the data to stabilize variance $\log(X + 1)$, and 4) selecting the top highly variable genes (HVGs).

UMAP Visualization parameters

In Table S4 are described the minimum distance and nearest neighbors choices for UMAP visualizations.

Dataset	UMAP parameters	AE	AEC	MEDL-AE-FE	MEDL-AEC-FE	MEDL-AE-RE
Healthy Heart	Min distance			0.5		0
	Nearest Neighbors			15		1000
ASDc	Min distance			0.5		
	Nearest Neighbors			15		
AMLh	Min distance			0.5		
	Nearest Neighbors			15		

Hardware

Our MEDL subnetworks, particularly the Random Effects subnetwork, are complex models that require graphics processing unit (GPU) for training. We used a Tesla V100 GPU with 32GB of memory and Tesla P4 GPU with 8GB of memory to train our models. However, the Fixed Effects subnetworks and autoencoder models are less computationally demanding and can be trained on the Tesla P4 GPU with 8GB of memory.

Supplemental Results

Supplementary Figures for Dataset Description

Donor Representation Across Cell Types in AMLh dataset

Fig. S1 illustrates the distribution of donors across each cell type. As observed, not all donor samples contain cells from every cell type, leading to potential confounding between donor identity and cell type.

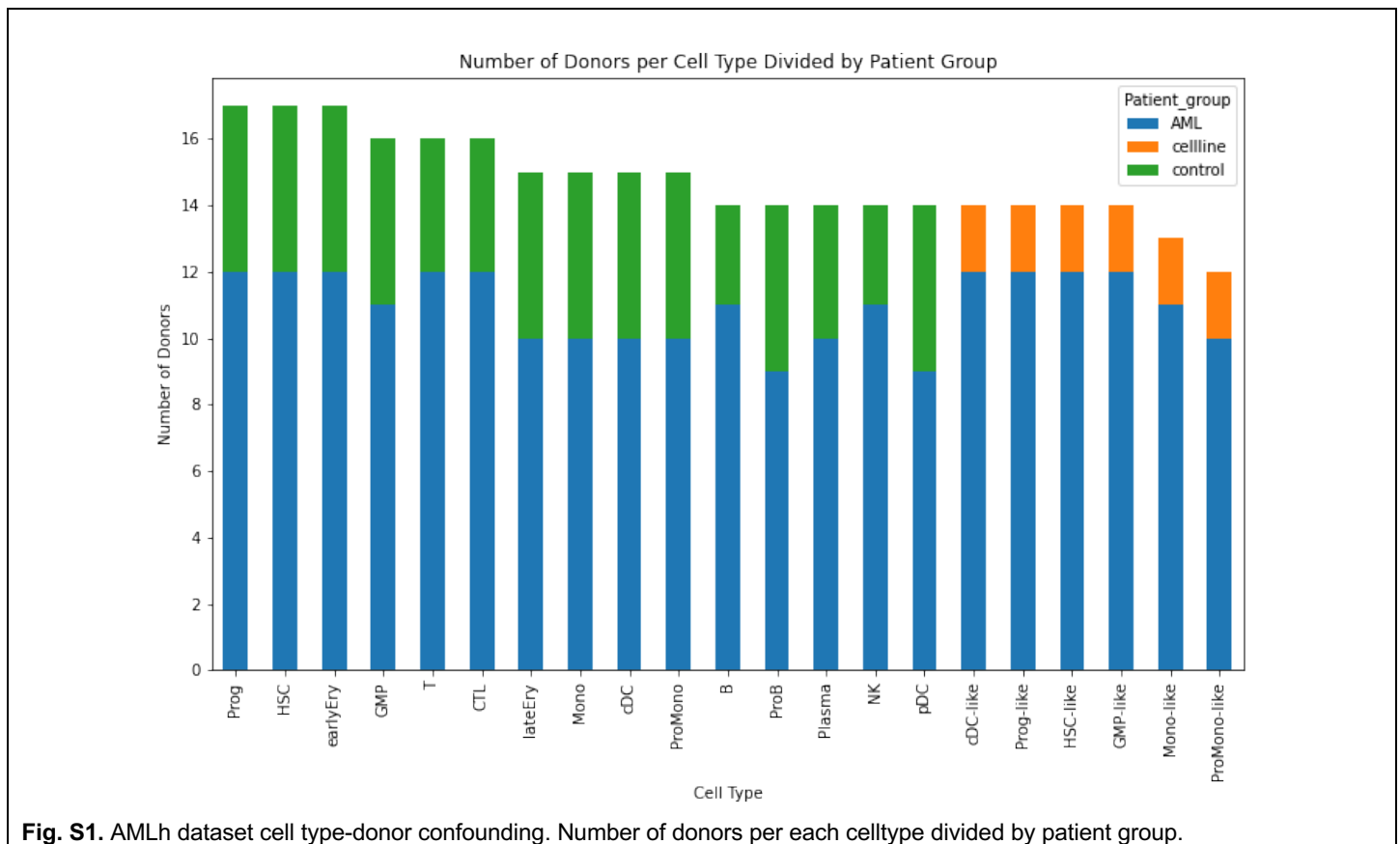


Fig. S1. AMLh dataset cell type-donor confounding. Number of donors per each celltype divided by patient group.

Hyperparameter Optimization for Experiments 1 A) and 3

ASW Scores for Batch and Cell Type Separability

Hyperparameter optimization (HPO) was conducted manually on a case-by-case basis to maximize the Average Silhouette Width (ASW) for cell type. Tables S5 and S6 present ASW scores for both batch and cell type separability for different values of the weights assigned to the reconstruction loss (mean squared error, MSE), adversarial loss, and classification loss of the cell type labels y . These results were derived from the validation sets of the ASDc and AMLh datasets.

Table S5. Average Silhouette Width (ASW) Scores for Batch and Cell Type Separability of **ASDc dataset** (Mean Across 5 Folds). Hyperparameter Optimization (HPO) on reconstruction loss weight λ_{MSE} on validation dataset. Adversarial loss weight $\lambda_A = 1$ for all models.

	λ_{MSE}	λ_A	ASW (batch)			ASW (cell type)		
			mean	95% CI		mean	95% CI	
MEDL-AE-FE	10	1	-0.27	-0.35	-0.19	0.01	-0.10	0.12
MEDL-AE-FE	100		-0.27	-0.32	-0.21	0.08	0.04	0.12
MEDL-AE-FE	1000		-0.23	-0.28	-0.19	0.20	0.16	0.24

Table S6. Average Silhouette Width (ASW) Scores for Batch and Cell Type Separability of the **AMLh dataset** (Mean Across 5 Folds). Hyperparameter Optimization (HPO) on reconstruction loss λ_{MSE} and classification loss λ_{CCE_y} weights for validation. Adversarial loss weight $\lambda_A = 1$ for all models.

	λ_{MSE}	λ_{CCE_y}	ASW (batch)			ASW (cell type)		
			mean	95% CI		mean	95% CI	
MEDL-AE-FE	100	NA	-0.24	-0.25	-0.23	-0.14	-0.17	-0.11
MEDL-AE-FE	500		-0.28	-0.30	-0.26	-0.12	-0.15	-0.08
MEDL-AE-FE	1000		-0.30	-0.33	-0.28	-0.12	-0.13	-0.10
MEDL-AE-FE	2000		-0.28	-0.30	-0.27	-0.10	-0.13	-0.08
MEDL-AE-FE	3000		-0.28	-0.30	-0.27	-0.06	-0.08	-0.04
MEDL-AE-FE	4000		-0.29	-0.31	-0.28	-0.05	-0.07	-0.04
AEC	1	0.1	-0.43	-0.52	-0.34	-0.15	-0.23	-0.06
AEC	10		-0.37	-0.44	-0.31	-0.11	-0.20	-0.02
AEC	100		-0.28	-0.34	-0.23	0.03	-0.04	0.10
MEDL-AEC-FE	500	1	-0.33	-0.35	-0.31	-0.10	-0.13	-0.06
MEDL-AEC-FE	1500	1	-0.30	-0.37	-0.24	-0.05	-0.08	-0.02
MEDL-AEC-FE	1500	2	-0.33	-0.40	-0.26	-0.07	-0.11	-0.04
MEDL-AEC-FE	2000	2	-0.31	-0.33	-0.28	-0.07	-0.13	-0.01

Supplementary Results for Experiment 1 A)

CH and 1/DB scores

In tables S7-S9, the CH and 1/DB scores are bolded when they correspond to the top-ranked model based on the ASW result, even if their values differ. The bolding indicates that, despite variations in the CH and 1/DB values, these models maintain the top performance ranking across all metrics for cell type preservation.

Table S7. 1/DB and CH scores (Mean and 95% CI across 5 folds) for batch and cell type separability in the latent spaces of the Healthy Heart Dataset, using PCA, AE, MEDL-AE-FE, and MEDL-AE-RE models.

	batch						cell type					
	1/DB			CH			1/DB			CH		
	mean	95% CI		mean	95% CI		mean	95% CI		mean	95% CI	
PCA (Baseline)	0.02	0.01	0.03	148.65	145.33	151.98	0.13	0.10	0.15	1502.74	1456.79	1548.69
AE	0.02	0.02	0.02	70.49	51.09	89.90	0.22	0.10	0.33	1712.76	1405.70	2019.83
MEDL-AE-FE	0.02	0.01	0.02	61.38	38.74	84.03	0.19	0.13	0.24	1984.01	1078.08	2889.95
MEDL-AE-RE	0.56	0.17	0.94	2555.27	544.02	4566.51	0.06	0.04	0.08	224.76	66.19	383.34

Table S8. 1/DB and CH scores (Mean and 95% CI across 5 folds) for batch and cell type separability in the latent spaces of the ASDc Dataset, using PCA, AE, MEDL-AE-FE, and MEDL-AE-RE models.

	batch						cell type					
	1/DB			CH			1/DB			CH		
	mean	95% CI		mean	95% CI		mean	95% CI		mean	95% CI	
PCA (Baseline)	0.03	0.02	0.03	32.67	32.06	33.28	0.18	0.15	0.21	9089.94	8906.86	9273.02
AE	0.02	0.02	0.03	23.72	20.74	26.69	0.78	0.71	0.85	9863.14	8673.06	11053.22
MEDL-AE-FE	0.02	0.02	0.03	19.43	14.12	24.74	0.32	0.15	0.49	9631.75	8052.25	11211.25
MEDL-AE-RE	0.16	-0.09	0.40	2423.99	-3510.80	8358.77	0.03	0.01	0.04	749.41	-261.64	1760.45

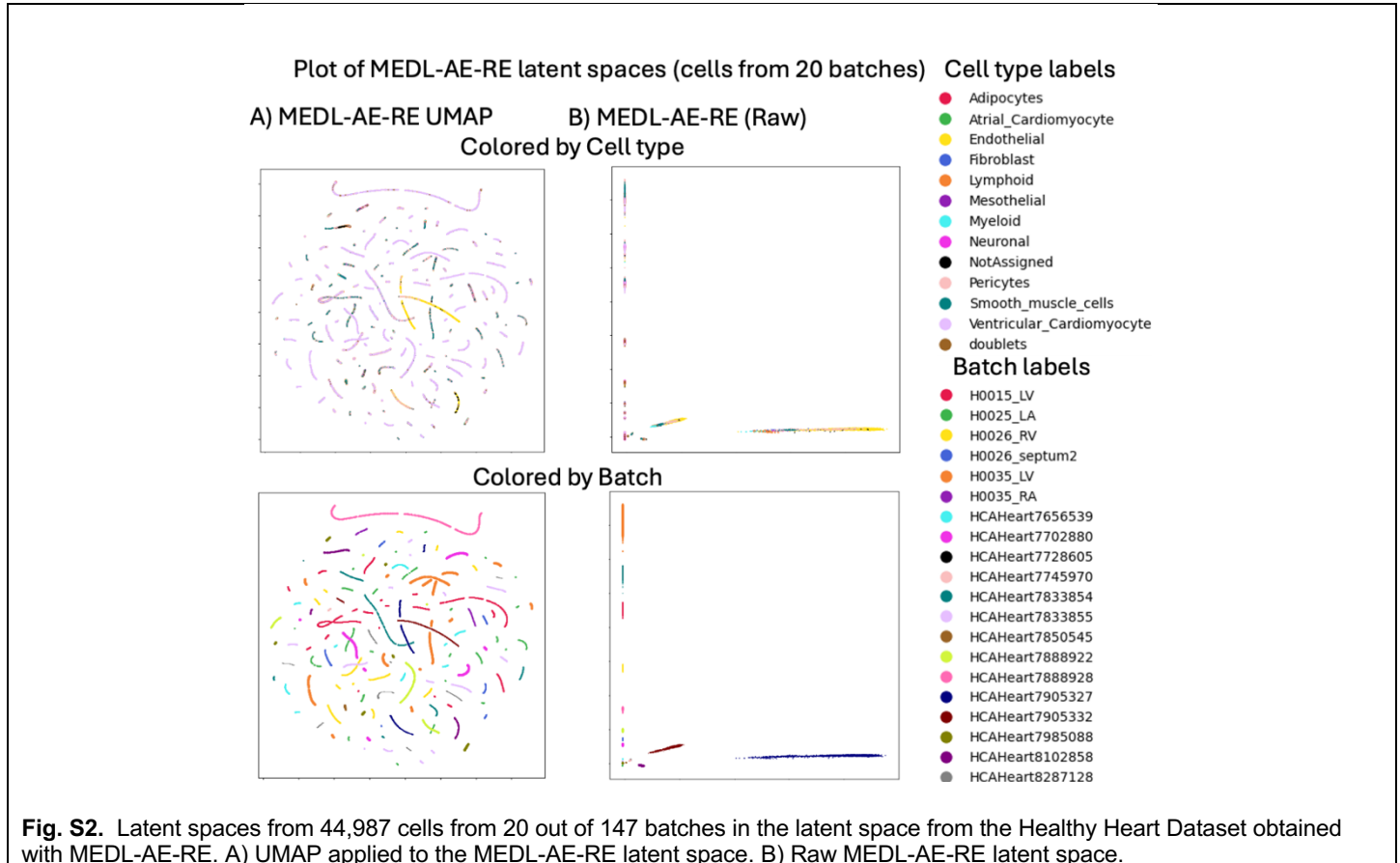
Table S9. 1/DB and CH scores (Mean and 95% CI across 5 folds) for batch and cell type separability in the latent spaces of the AMLh Dataset, using PCA, AE, MEDL-AE-FE, and MEDL-AE-RE models.

	batch						cell type					
	1/DB			CH			1/DB			CH		
	mean	95% CI		mean	95% CI		mean	95% CI		mean	95% CI	
PCA (Baseline)	0.06	0.05	0.07	156.52	154.20	158.84	0.14	0.12	0.16	2560.96	2482.14	2639.79
AE	0.07	0.07	0.08	189.78	169.23	210.32	0.28	0.24	0.32	1956.48	1779.39	2133.58
MEDL-AE-FE	0.07	0.06	0.09	80.63	69.88	91.37	0.19	0.09	0.29	1493.43	1353.85	1633.01
MEDL-AE-RE	0.37	0.07	0.67	63228.21	9245.17	117211.25	0.07	0.05	0.09	114.73	69.53	159.94

Random Effects Subnetwork (MEDL-AE-RE) latent spaces

Fig. S2–S4 illustrate the MEDL-AE-RE latent spaces using two visualization methods: (A) UMAP applied to the MEDL-AE-RE latent representations and (B) the raw MEDL-AE-RE representations. The UMAP visualizations introduce artifacts due to outliers present in the batch distributions. Specifically:

- Fig. S2 shows the latent space for the Healthy Heart dataset.
- Fig. S3 presents the latent space for the ASDc dataset.
- Fig. S4 depicts the latent space for the AMLh dataset.



Plot of MEDL-AE-RE latent spaces (cells from 31 batches)

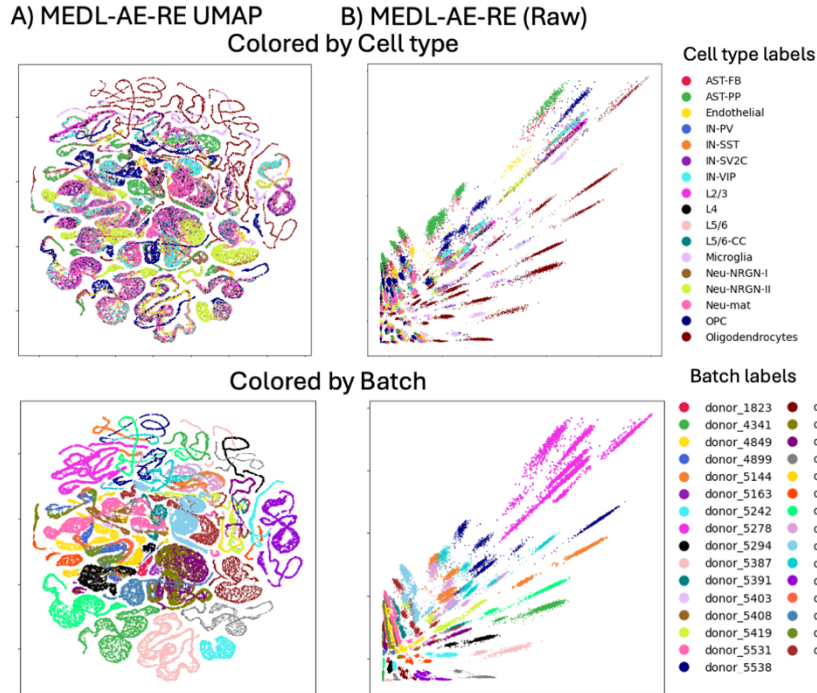


Fig. S3. Latent spaces from 62735 cells from ASDc dataset latent spaces obtained with MEDL-AE-RE. A) UMAP applied to the MEDL-AE-RE latent space. B) Raw MEDL-AE-RE latent space.

Plot of MEDL-AE-RE latent spaces (cells from 19 batches)

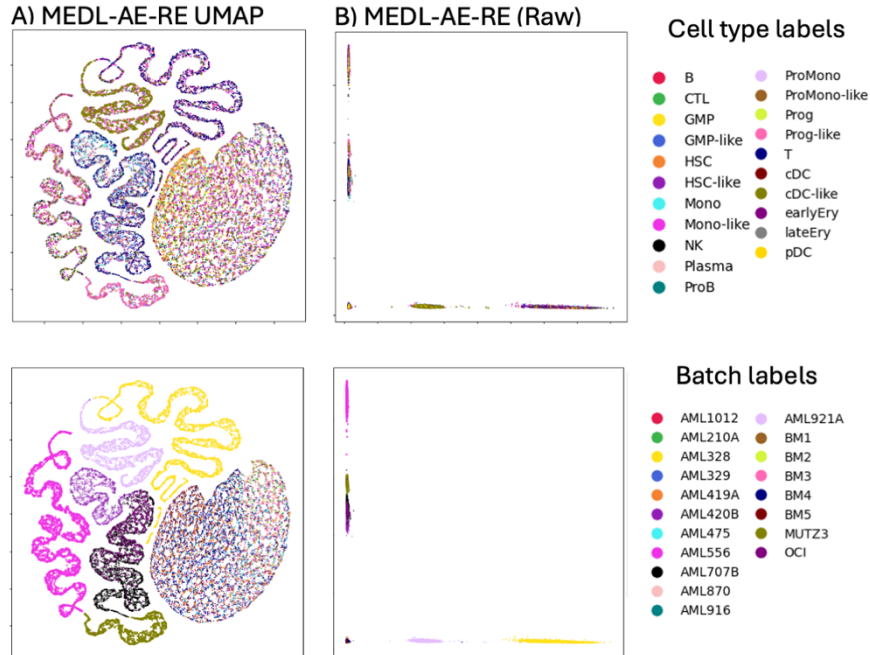


Fig. S4. Latent spaces from 23,050 cells from the AMLh dataset latent spaces obtained with MEDL-AE-RE. A) UMAP applied to the MEDL-AE-RE latent space. B) Raw MEDL-AE-RE latent space.

Average Training and Validation Curves for AE, MEDL-AE-FE, and MEDL-AE-RE Across 5 Folds in the Healthy Heart, ASDc, and AMLh Datasets

Fig. S5-S7 present the training and validation curves, weighted accordingly, for the AE, MEDL-AE-FE, and MEDL-AE-RE models in all three datasets. For MEDL-AE-FE, the total loss is calculated as the reconstruction loss minus the adversarial loss, with each component adjusted by its respective weight. In the MEDL-AE-RE curves, the left axis displays the reconstruction loss and total loss, while the right axis represents the latent cluster loss, which classifies batch effects, and the Kullback-Leibler divergence (KLD) loss. The total loss is computed as the sum of the reconstruction loss, latent cluster loss, and KLD loss, each adjusted by their respective weights.

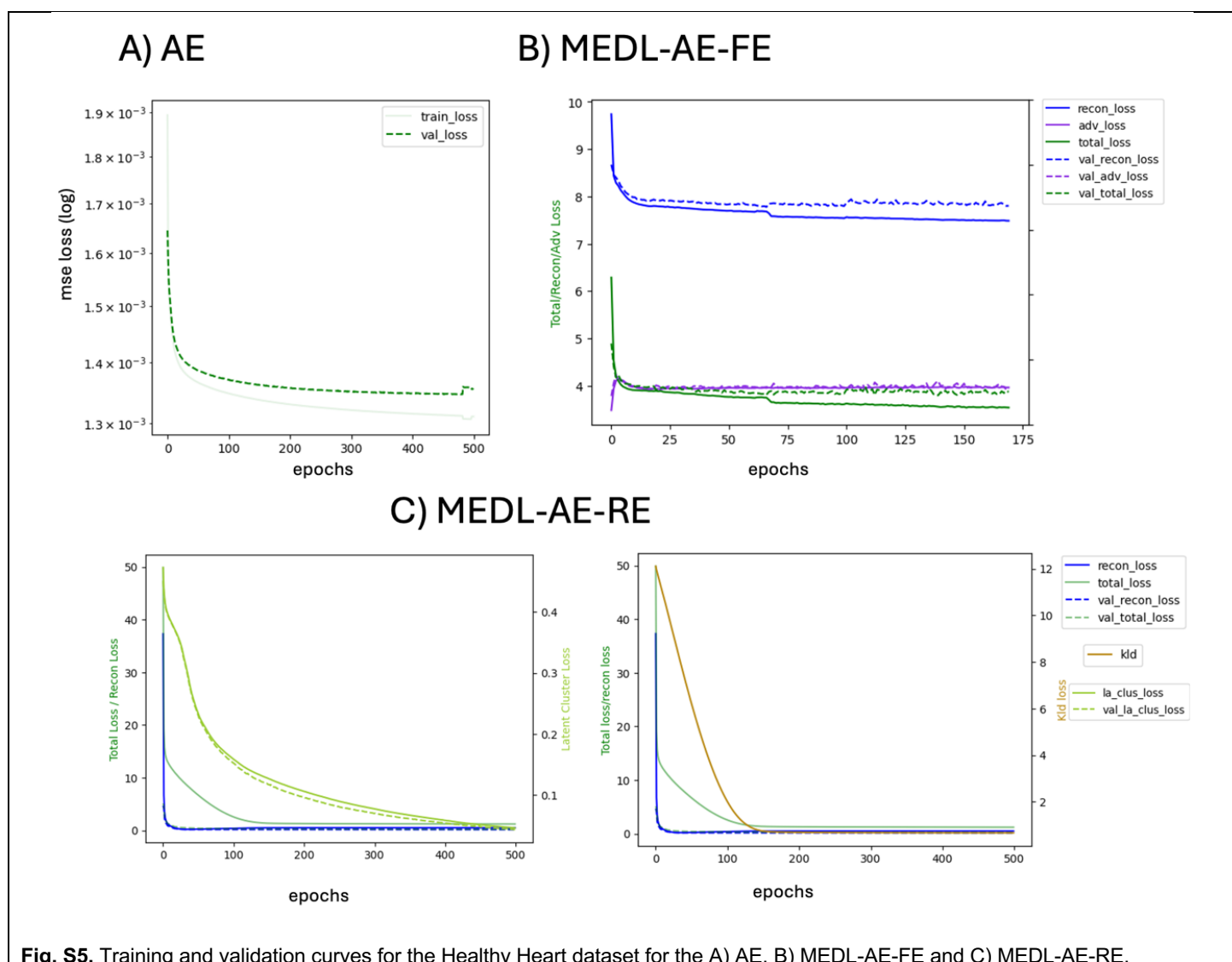


Fig. S5. Training and validation curves for the Healthy Heart dataset for the A) AE, B) MEDL-AE-FE and C) MEDL-AE-RE.

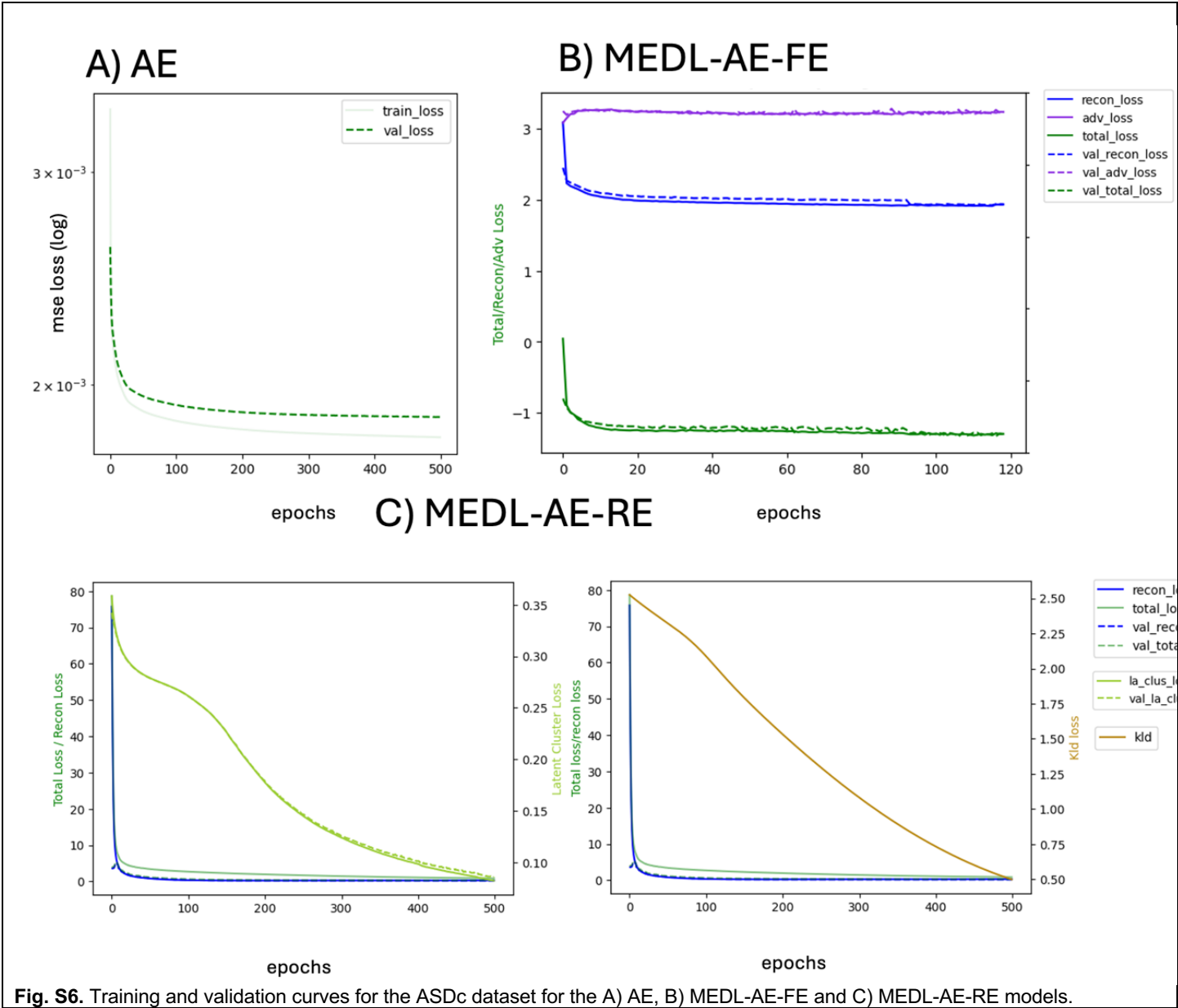
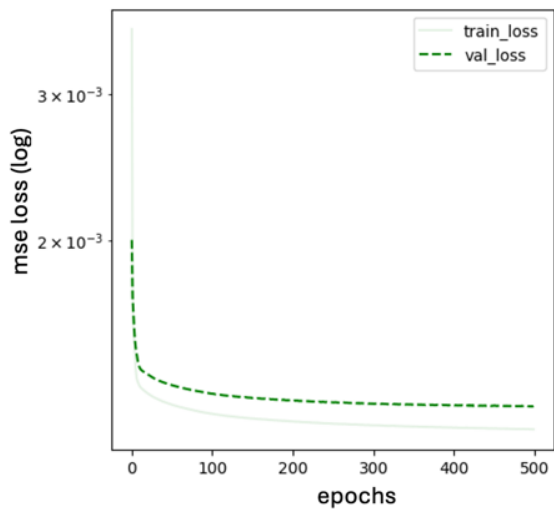
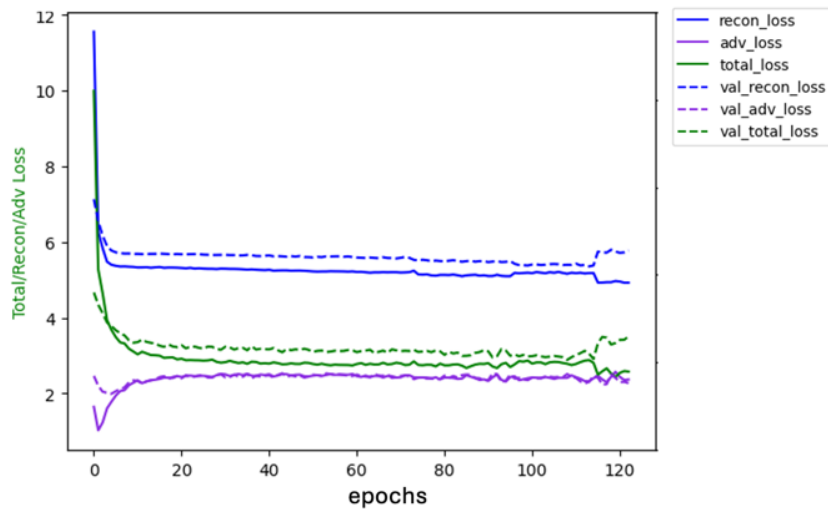


Fig. S6. Training and validation curves for the ASDc dataset for the A) AE, B) MEDL-AE-FE and C) MEDL-AE-RE models.

A) AE



B) MEDL-AE-FE



C) MEDL-AE-RE

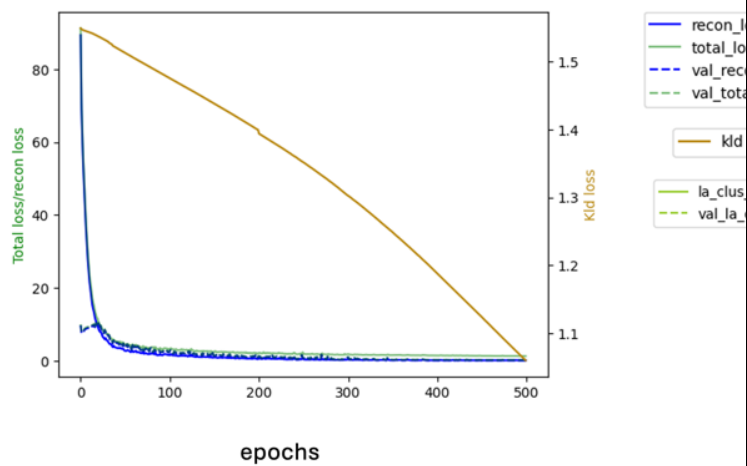
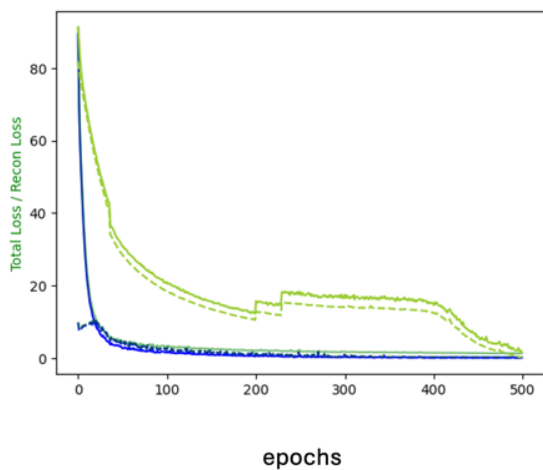


Fig. S7. Training and validation curves for the AMLh dataset for the A) AE, B) MEDL-AE-FE and C) MEDL-AE-RE models.

Supplementary Results for Experiment 3

CH and 1/DB scores

In tables S10-S12, the CH and 1/DB scores are bolded when they correspond to the top-ranked model based on the ASW result, even if their values differ. The bolding indicates that, despite variations in the CH and 1/DB values, these models maintain the top performance ranking across all metrics for cell type preservation.

Table S10. 1/DB and CH scores (Mean and 95% CI across 5 folds) for batch and cell type separability in the latent spaces of the Healthy Heart Dataset, using AEC and MEDL-AEC-FE models.

	batch						cell type					
	1/DB			CH			1/DB			CH		
	mean	95% CI		mean	95% CI		mean	95% CI		mean	95% CI	
AEC	0.02	0.01	0.03	48.29	15.26	81.32	0.23	0.06	0.41	5563.96	2833.93	8293.99
MEDL-AEC-FE	0.02	0.01	0.02	41.39	27.01	55.77	0.21	0.04	0.38	3750.68	2318.16	5183.19

Table S11. 1/DB and CH scores (Mean and 95% CI across 5 folds) for batch and cell type separability in the latent spaces of the ASDc Dataset, using AEC and MEDL-AEC-FE models.

	batch						cell type					
	1/DB			CH			1/DB			CH		
	mean	95% CI		mean	95% CI		mean	95% CI		mean	95% CI	
AEC	0.02	0.01	0.03	20.06	14.48	25.64	0.73	0.51	0.95	10631.01	5846.41	15415.61
MEDL-AEC-FE	0.02	0.01	0.02	12.72	7.40	18.03	0.34	0.18	0.50	9911.04	8726.06	11096.02

Table S12. 1/DB and CH scores (Mean and 95% CI across 5 folds) for batch and cell type separability in the latent spaces of the AMLh, using AEC and MEDL-AEC-FE models.

	batch						cell type					
	1/DB			CH			1/DB			CH		
	mean	95% CI		mean	95% CI		mean	95% CI		mean	95% CI	
AEC	0.08	0.04	0.12	142.75	81.95	203.54	0.17	0.09	0.25	2159.15	1216.68	3101.61
MEDL-AEC-FE	0.06	0.04	0.07	87.24	70.03	104.45	0.18	0.10	0.25	2065.85	1301.67	2830.04

Average Training and Validation Curves for AEC and MEDL-AEC-FE Across 5 Folds in the Healthy Heart, ASDc, and AMLh Datasets

Fig. S8-S10 present the training and validation curves, weighted accordingly, for the AEC and MEDL-AEC-FE models in all three datasets. For AEC the total loss is calculated as the sum of the reconstruction loss and the cell type classification loss, with each component adjusted by its respective weight. For MEDL-AEC-FE, the total loss is calculated as the sum of the reconstruction loss and the cell type classification loss minus the adversarial loss, with each component adjusted by its respective weight.

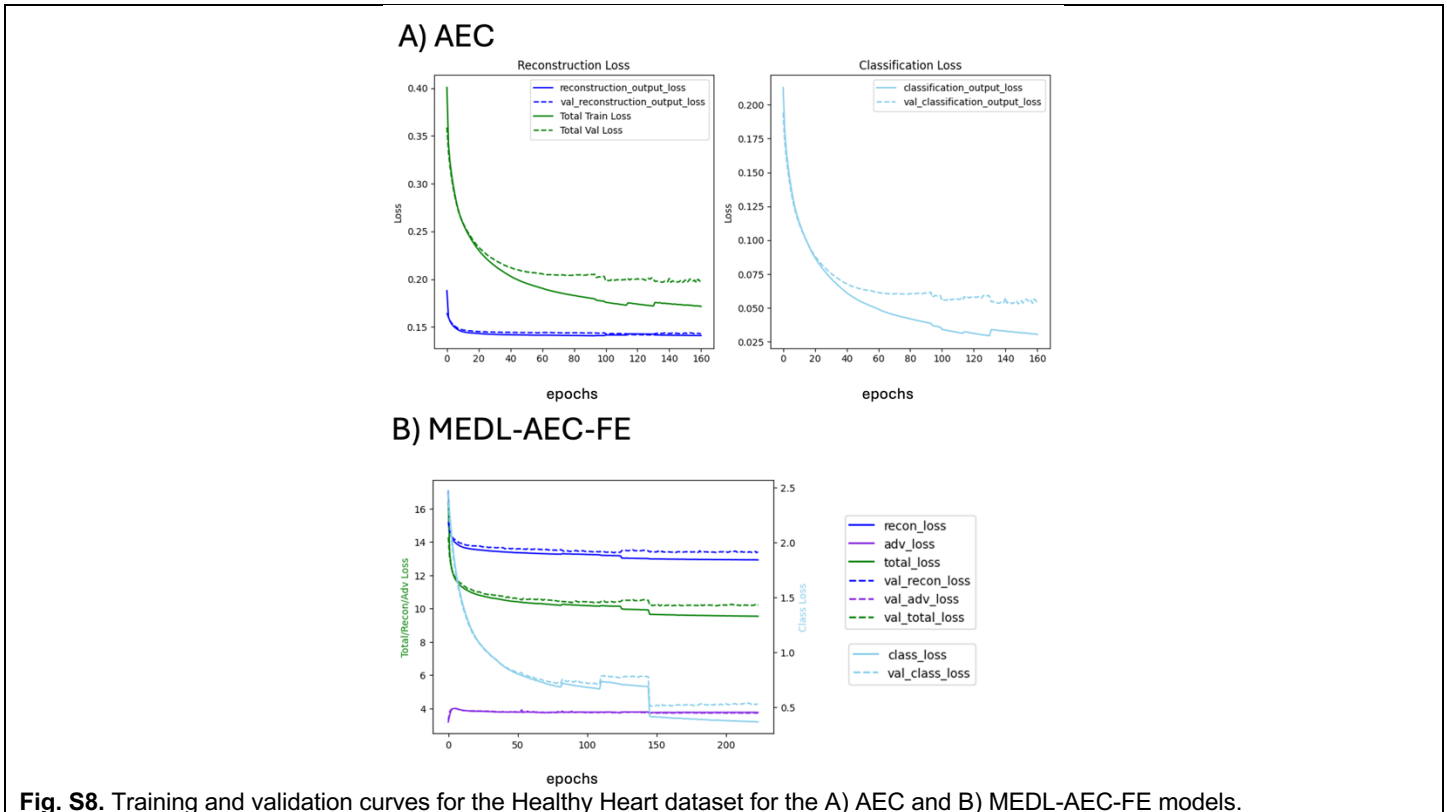
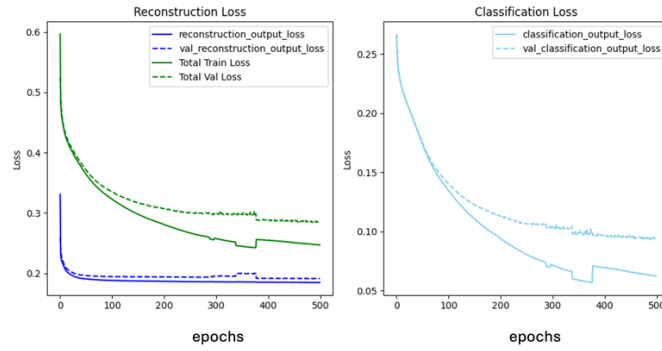


Fig. S8. Training and validation curves for the Healthy Heart dataset for the A) AEC and B) MEDL-AEC-FE models.

A) AEC



B) MEDL-AEC-FE

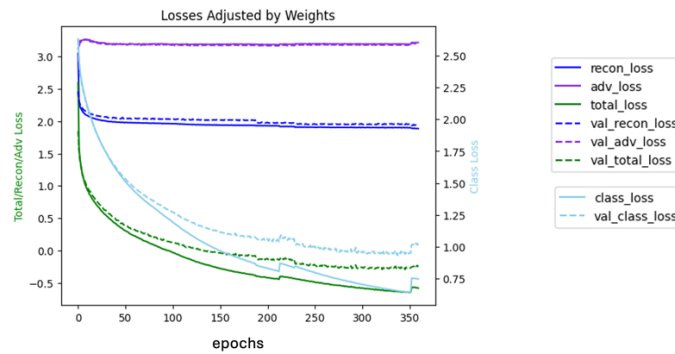
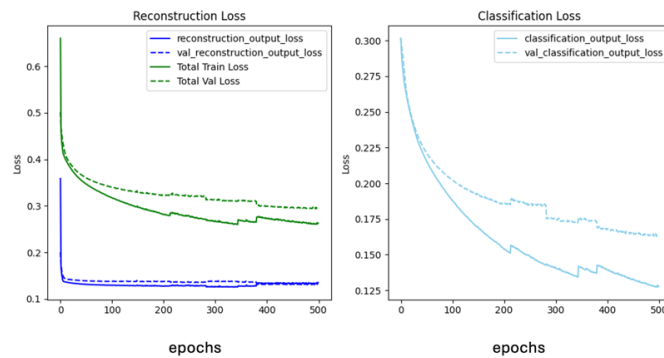


Fig. S9. Training and validation curves for the ASDc dataset for the A) AEC and B) MEDL-AEC-FE models.

A) AEC



B) MEDL-AEC-FE

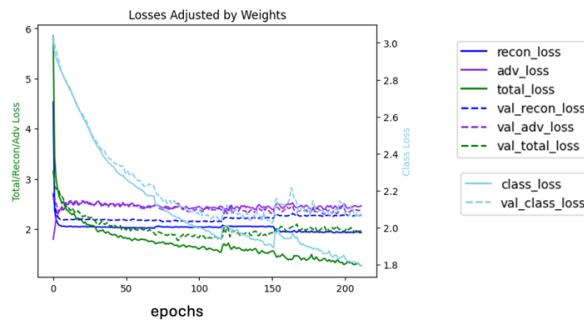


Fig. S10. Training and validation curves for the AMLh dataset for the A) AEC and B) MEDL-AEC-FE models.

References

Yu, X., Xu, X., Zhang, J., & Li, X. (2023). Batch alignment of single-cell transcriptomics data using deep metric learning. *Nat Commun*, 14(1), 960. <https://doi.org/10.1038/s41467-023-36635-5>